EES Batteries

ROYAL SOCIETY OF CHEMISTRY

REVIEW

View Article Online
View Journal | View Issue

Cite this: *EES Batteries*, 2025, **1**, 744

Electronic modulation strategies for enhanced cathode catalysis in lithium–oxygen batteries: challenges, advancements, and future perspectives

Mengyao Huang,[a,b] Kwan San Hui, *[c] Qingchao Liu, [b] Fuming Chen, [d] Sambasivam Sangaraju [e] and Kwun Nam Hui *[a]

Lithium–oxygen (Li–O_2) batteries have emerged as a promising rechargeable energy storage technology, offering exceptionally high theoretical energy density, which makes them attractive for applications in electric vehicles, renewable energy storage, and portable devices. Despite their potential, the practical application of Li–O_2 batteries is significantly hindered by challenges such as high overpotential, low discharge capacity, poor rate capability, and unstable cycle life. These issues primarily arise from the insulating nature of the discharge product (Li_2O_2) and the sluggish electrochemical kinetics of the oxygen reduction reaction (ORR) and oxygen evolution reaction (OER). Addressing these challenges requires the development of efficient and stable cathode catalysts. Recent advancements in cathode catalyst design have provided valuable insights into the structure–performance relationship, especially regarding how electronic modulation can enhance catalytic efficiency. This review systematically examines the challenges, recent advancements, and future perspectives of cathode catalyst design for Li–O_2 batteries. Particular emphasis is placed on understanding how the electronic properties of catalysts influence battery performance and exploring innovative strategies, such as external-field-assisted catalysis, to optimize catalytic activity. Furthermore, the review discusses future research directions, including precise molecular and atomic-level modulation of catalyst electronic structures, advanced *in situ* characterization techniques, and the synergistic optimization of electrode/electrolyte interfaces, aiming to provide theoretical guidance for developing high-performance Li–O_2 batteries.

Received 28th March 2025,
Accepted 4th May 2025

DOI: 10.1039/d5eb00060b

rsc.li/EESBatteries

Broader context

Lithium–oxygen (Li–O_2) batteries, with their remarkably high theoretical energy density, are at the forefront of next-generation energy storage technologies. As the demand for sustainable energy solutions grows, particularly for electric vehicles and grid-scale storage, Li–O_2 batteries offer a promising alternative to conventional lithium-ion systems. However, their practical application remains hampered by fundamental challenges, including high overpotential, poor cycle stability, and low efficiency due to the insulating nature of lithium peroxide (Li_2O_2) and sluggish oxygen redox reactions. Recent progress in catalyst development, particularly through electronic modulation strategies, has opened new avenues for enhancing catalytic activity, stability, and overall battery performance. This review provides a comprehensive analysis of these advancements, offering insights that could pave the way for more efficient, durable, and scalable Li–O_2 battery systems. By addressing the key challenges and identifying future research directions, this work contributes to the broader effort of making high-energy-density batteries viable for real-world applications.

1. Introduction

Lithium–oxygen (Li–O_2) batteries have garnered significant attention as a next-generation energy storage technology due to their exceptionally high theoretical energy density (up to 3500 W h kg^{-1}). This remarkable energy density positions them as transformative solutions for electric vehicles, grid-scale energy storage systems, and portable electronics.[1] Compared to conventional lithium-ion batteries (LIBs),[2–4] Li–O_2 batteries offer a promising pathway towards sustainable and efficient energy storage. However, the practical deploy-

[a]*Joint Key Laboratory of the Ministry of Education, Institute of Applied Physics and Materials Engineering, University of Macau, Avenida da Universidade, Taipa, Macau SAR, China. E-mail: bizhui@um.edu.mo*
[b]*College of Chemistry, Zhengzhou University, Zhengzhou 450001, P.R. China*
[c]*Department of Mechanical Engineering, College of Engineering, Prince Mohammad Bin Fahd University, P.O. Box 1664, Al Khobar 31952, Kingdom of Saudi Arabia. E-mail: khui@pmu.edu.sa*
[d]*School of Chemistry and Chemical Engineering, Hainan University, Haikou, 570228, China*
[e]*National Water and Energy Center, United Arab Emirates University, Al Ain-15551, United Arab Emirates*

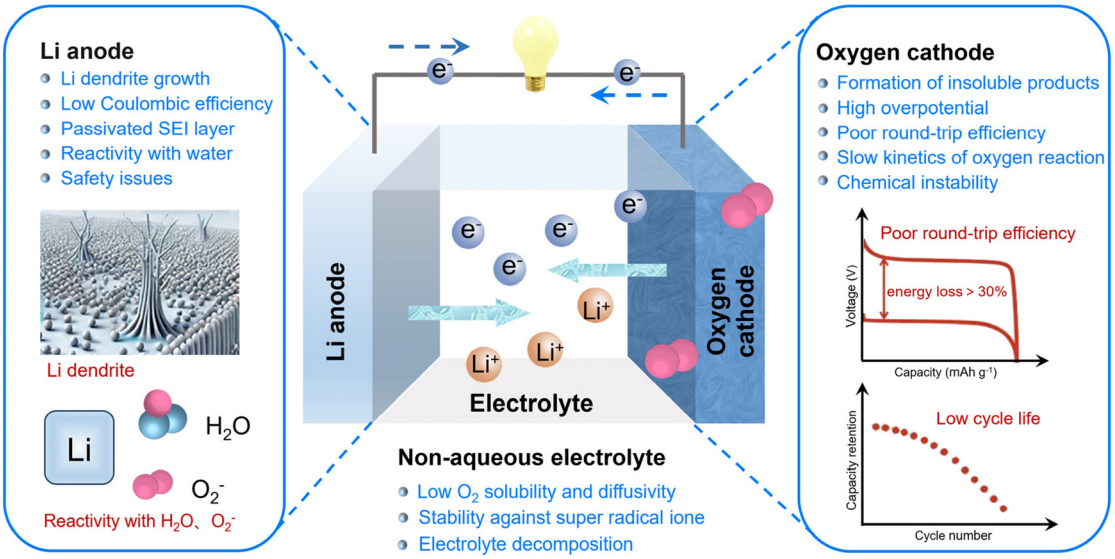

Fig. 1 Major challenges for the rechargeable Li–O_2 battery.

ment of Li–O_2 batteries faces several critical challenges that hinder their large-scale application. These challenges primarily stem from the complex electrochemical processes at the cathode, where the formation of insulating lithium peroxide (Li_2O_2) during discharge and its sluggish decomposition during charging result in high overpotential and limited cycle life.[5–10]

Despite the impressive theoretical energy density of Li–O_2 batteries, their practical application is significantly constrained by the intricate interplay of multi-scale electrochemical processes (Fig. 1). At the cathode interface, the wide band gap and insulating nature of the discharge product Li_2O_2 pose substantial obstacles to electron and ion transport during both charge and discharge cycles, leading to interface passivation.[11,12] Consequently, the kinetics of the ORR and OER in Li–O_2 batteries are relatively slow, leading to increased charge/discharge polarization and a decline in energy efficiency (<65%). Existing cathode materials struggle to maintain high activity over long cycles. Additionally, high costs and limited material availability, particularly the reliance on noble metal catalysts[13–15] and scarce carbon materials,[13,16–18] hinder large-scale application. During dynamic cycling, the disproportionation of Li_2O_2 and the generation of singlet oxygen ($^1O_2$) can cause electrolyte decomposition, forming byproducts such as Li_2CO_3 and carboxylic acids in ether-based electrolytes.[19,20] This process leads to cathode pore blockage and interfacial failure. At charging voltages exceeding 3.4 V, the electrochemical decomposition of LiO_2 or Li_2O_2 further generates $^1O_2$, and the auto-oxidation of superoxide species and O_2 has been identified as a common mechanism of electrolyte degradation. Solid-state electrolytes have garnered considerable attention due to their enhanced chemical stability; however, they continue to face challenges related to poor ionic conductivity. A critical issue concerning the lithium anode is the

Mengyao Huang

Meng-Yao Huang received her master's degree from the Department of Chemistry at Zhengzhou University in 2025. She is currently pursuing her Ph. D. at the Institute of Applied Physics and Materials Engineering, University of Macau, under the supervision of Prof. Kwun Nam Hui. Her research focuses on the design and mechanistic study of cathode catalysts and electrolyte additives in metal–air batteries.

Kwan San Hui

Kwan San Hui is a Full Professor in the Department of Mechanical Engineering at the College of Engineering, Prince Mohammad Bin Fahd University. He earned his Ph.D. in Mechanical Engineering from the Hong Kong University of Science and Technology in 2008. His research interests include advanced materials for energy storage, energy conversion, and electrocatalysis. He is a Fellow of both the Royal Society of Chemistry (UK) and the Higher Education Academy (UK).

undesirable morphological evolution during repeated lithium plating and stripping.[21,22] In particular, at higher current densities, lithium metal surfaces can develop mossy (dense, porous microstructures) and dendritic (sharp, outward-protruding) growth. Dendritic growth can lead to electrical short circuits in the battery, posing severe safety risks if the lithium dendrites penetrate the separator and contact the O_2 electrode. Additionally, the formation of mossy structures results in low coulombic efficiency due to the continuous formation of new solid electrolyte interphase (SEI) layers on the increased lithium surface area.[23] Moreover, the emergence of electrically isolated lithium structures renders portions of the lithium metal electrochemically inactive. These challenges fundamentally stem from the suboptimal regulation of electrode/electrolyte interfacial reaction pathways.

In recent years, with advancements in materials science and electrochemical theory, significant breakthroughs have been made in the design and optimization of Li–O_2 batteries.[5,42–45] Notably, substantial progress has also been achieved in the field of cathode catalysis (Fig. 2). The rational design and precise control of catalysts with excellent reaction kinetics, reversibility, and high ORR/OER activity are crucial for advancing the practical application of Li–O_2 batteries. Breakthroughs in density functional theory (DFT) calculations and *in situ* characterization techniques have enabled researchers to progressively elucidate the structure–activity relationship between catalyst electronic properties and ORR/OER kinetics.[46,47] This provides critical theoretical support for advancing Li–O_2 battery technology and its practical applications. This review begins by examining the fundamental charge–discharge mechanisms of Li–O_2 batteries and the critical role of cathode catalysts. It discusses the charge transfer mechanisms at the electrolyte-Li_2O_2-cathode interface and integrates recent advancements in cathode catalyst design, with a particular focus on the influence of catalyst electronic properties on catalytic activity (Fig. 3). A systematic analysis is provided on various tuning strategies, including d-band center modulation in metals, optimization of p-band non-metallic sites, occupancy of e_g orbitals, orbital hybridization, exposed crystal facet engineering, and external-field-assisted innovations, all of which contribute to enhancing catalytic performance. Finally, the current state of cathode catalyst design for Li–O_2 batteries is discussed, along with perspectives on future research. This review provides theoretical insights and guidance for the design and further optimization of advanced cathode catalysts.

2. Mechanism and charge transport path of Li–O_2 battery

2.1 Mechanism for Li–O_2 battery electrochemistry

The fundamental working mechanism of Li–O_2 batteries relies on the oxygen reduction reaction (ORR) and oxygen evolution reaction (OER),[54,55] which alternately occur during discharge and charge cycles to enable energy storage and release (eqn (1)).

$$2Li + O_2 \rightarrow Li_2O_2 \quad (E^\circ = 2.96\ V\ vs.\ Li/Li^+) \qquad (1)$$

The discharge process of Li–O_2 batteries relies on the ORR at the cathode, wherein oxygen molecules are reduced to solid lithium peroxide (Li_2O_2) through a series of multi-step electron transfers (Fig. 4).[56] The specific reaction begins with the adsorption of O_2 molecules onto the cathode surface, followed by the acceptance of an electron, forming superoxide ions (O_2^-) (eqn (2)). The kinetics of this step are significantly influenced by the oxygen concentration in the electrolyte and the surface activity of the catalyst. O_2^- ions then combine with Li^+ from the anode to form an intermediate product, LiO_2. The stability of LiO_2 is contingent upon the donor number (DN) of the electrolyte solvent[57,58] and the adsorption strength (ΔE_{ads}) of the cathode catalyst. In low-DN solvents (*e.g.*, TEGDME), the solvation of Li^+ in the electrolyte is weak, leading to a tendency for LiO_2 to undergo secondary electrochemical reduction or disproportionation reactions at the electrode surface (eqn (3)–(5)). Conversely, in high-DN solvents (*e.g.*, DMSO), facilitate the effective solvation of Li^+, enabling LiO_2 to dissolve into the

Qingchao Liu

Qingchao Liu received his M.E. and Ph.D. degrees in Materials Science from Jilin University, Changchun, China, in 2012 and 2015, respectively. He is currently working at Zhengzhou University, China. His research focuses on the design and synthesis of functional materials for energy storage and catalysis.

Fuming Chen

Fuming Chen is a Professor at South China Normal University. He received his Ph.D. from Nanyang Technological University, Singapore, in 2011. His current research focuses on advanced functional materials for electrochemical energy storage and desalination.

electrolyte and undergo disproportionation reactions, resulting in the formation of toroidal Li_2O_2 particles (eqn (6) and (7)).

$$O_{2(g)} + e^- \rightarrow O_2{}^-{}_{(sol)} \quad (2)$$

$$Li^+{}_{(sol)} + O_2{}^-{}_{(sol)} \rightarrow LiO_{2(sol)} \quad (3)$$

$$2LiO_{2(sol)} \rightarrow Li_2O_{2(sol)} + O_{2(g)} \quad (4)$$

$$Li^+{}_{(sol)} + e^- + O_2 \rightarrow LiO_{2(ads)} \quad (5)$$

$$Li^+{}_{(sol)} + e^- + LiO_{2(ads)} \rightarrow Li_2O_{2(ads)} \quad (6)$$

$$2LiO_{2(ads)} \rightarrow Li_2O_{2(ads)} + O_{2(g)} \quad (7)$$

During the charging process, the decomposition of Li_2O_2 plays a critical role in energy storage (Fig. 5). This process involves the OER, whose sluggish kinetics lead to a high overpotential (typically >1 V), which is a fundamental issue limiting the efficiency of the battery.[55,59] The mechanism of OER is complex, and the reaction pathway, as well as the presence of intermediates, remains a subject of ongoing debate. Peng *et al.* used *in situ* surface-enhanced Raman spectroscopy (SERS) to monitor the charging process and found that the oxidation of Li_2O_2 did not exhibit characteristic peaks for the LiO_2 intermediate (such as the O–O vibrational peak at 1130 cm^{-1}).[60] They proposed that Li_2O_2 decomposes through a direct two-electron transfer pathway:

$$Li_2O_2 \rightarrow 2Li^+ + O_2 + 2e^-. \quad (8)$$

Further studies indicate that, similar to the discharge mechanism, oxidation pathway of Li_2O_2 during the charging process is influenced by the DN of the electrolyte solvent. During charging, Li_2O_2 first undergoes a delithiation reaction to form the $Li_{2-x}O_2$ intermediate (eqn (9)). In high-DN solvents, $Li_{2-x}O_2$ dissolves into LiO_2(sol) and subsequently undergoes disproportionation to generate O_2 (eqn (10) and (11)). In contrast, in low-DN solvents, the $Li_{2-x}O_2$ intermediate undergoes further oxidation *via* a solid-state mechanism to release O_2 (eqn (12)).

$$Li_2O_{2(s)} \rightarrow Li_{2-x}O_{2(s)} + xLi^+{}_{(sol)} + xe^- \quad (9)$$

$$Li_{2-x}O_{2(s)} \rightarrow LiO_{2(sol)} + (1-x)Li^+{}_{(sol)} + (1-x)e^- \quad (10)$$

$$2LiO_{2(sol)} \rightarrow Li_2O_{2(s)} + O_{2(g)} \quad (11)$$

$$Li_{2-x}O_{2(s)} \rightarrow O_{2(g)} + (2-x)Li^+{}_{(sol)} + (2-x)e^- \quad (12)$$

2.2 Reaction interfaces and electron transport pathways in charging and discharging processes

In Li–O_2 batteries, the electrolyte–catalyst interface is the core region where charge transport and ORR/OER occur, involving the adsorption, transport, dissociation of reactants, as well as the nucleation and decomposition of Li_2O_2.[61,62] The wide band gap characteristic of the Li_2O_2 discharge product leads to an extremely low intrinsic conductivity (σ_{ea} = 2.2 × 10^{-13} S cm^{-1}), and as discharge proceeds, both electron and ion transport become increasingly restricted.[63,64] Significant efforts have been made to study the active reaction interfaces and transport limitations during the charging and discharging processes of Li–O_2 batteries.[63,65–67]

Wang *et al.* conducted staged discharge experiments in tetraglyme electrolyte using isotope labeling, sequentially introducing $^{16}O_2$ and $^{18}O_2$.[48] Analysis using scanning electron microscopy (SEM) and time-of-flight secondary ion mass spectrometry (ToF-SIMS) revealed that the ring-shaped Li_2O_2 product exhibits a layered distribution, with $Li_2{}^{18}O_2$ enriched on the outer surface (electrolyte interface) and $Li_2{}^{16}O_2$ concentrated in the inner layer (electrode interface) (Fig. 6a). This finding supports the hypothesis that Li_2O_2 preferentially grows at the Li_2O_2-electrolyte interface. By reversing the isotope introduction sequence (introducing $^{18}O_2$ first, followed by $^{16}O_2$), the Li_2O_2 enrichment order was correspondingly reversed, further

Sambasivam Sangaraju

Sambasivam Sangaraju is a Senior Researcher at the National Water and Energy Center, United Arab Emirates University (UAE). He received his Ph.D. in Physics from Sri Venkateswara University, India, in 2008. He has held postdoctoral and associate professor positions in Taiwan, South Korea, Japan, the USA, China, India, and the UAE. His research mainly focuses on the development of high-performance nanostructured and nanocomposite materials based on super-thin, thin, and thick films, using novel and advanced material synthesis methods for applications in solar cells, energy storage, optoelectronics, magnetic materials, and hydrogen production.

Kwun Nam Hui

Kwun Nam Hui is an Associate Professor at the Institute of Applied Physics and Materials Engineering, University of Macau. He obtained his Ph.D. from The University of Hong Kong in 2009. His research focuses on developing new materials and understanding their properties for next-generation energy storage and conversion systems. He is a Fellow of the Royal Society of Chemistry (UK).

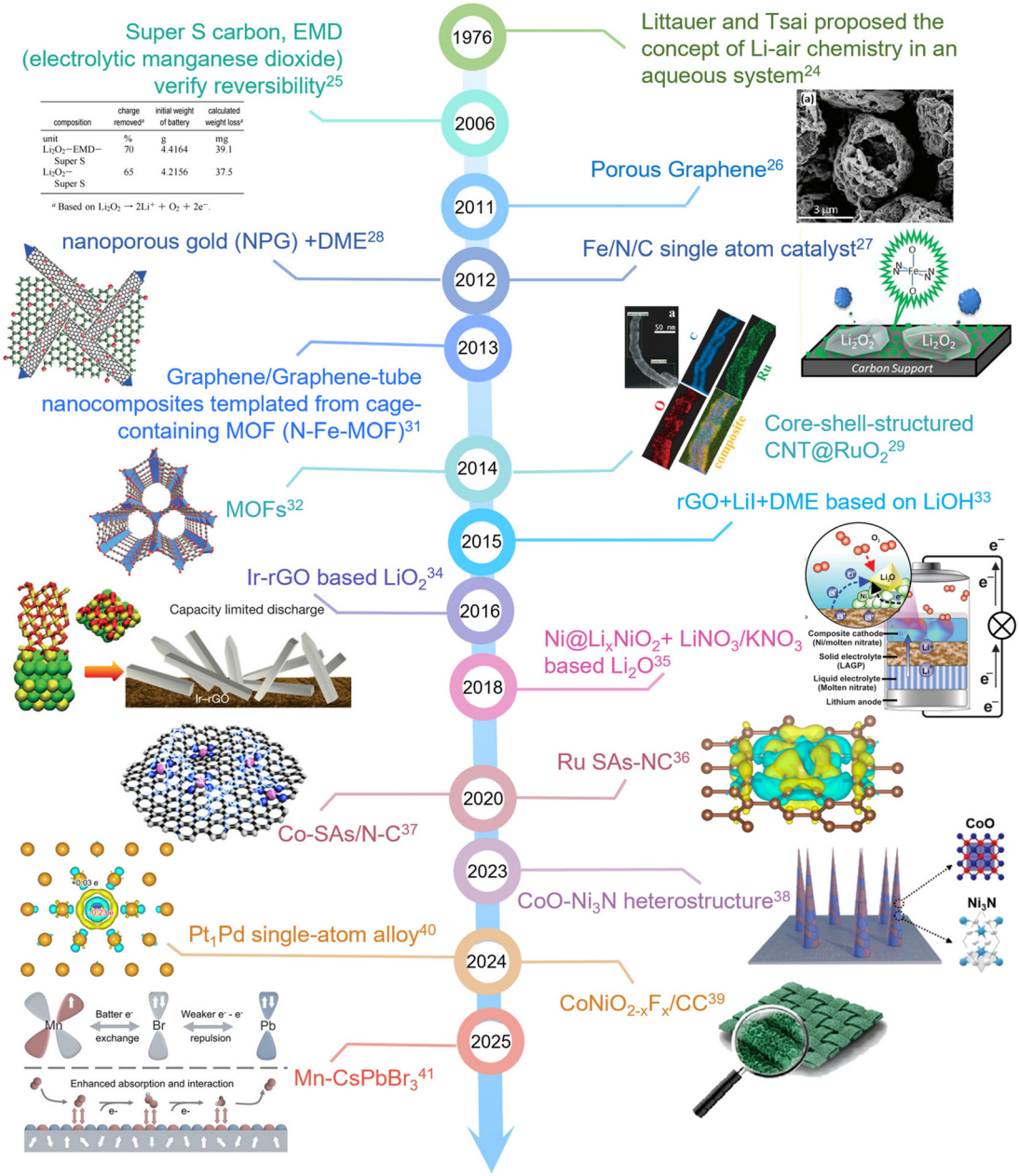

Fig. 2 Timeline of the development of Li–O_2 battery cathode catalysts.[24–41]

validating the correlation between oxygen evolution sequence and isotope distribution within Li_2O_2 particles. Wang *et al.* employed an Au electrode | Li_2O_2 thin film | Li^+/DMSO electrolyte system to *in situ* SERS. By discharging at a high current density (100 μA cm^{-2}), an ultrathin Li_2O_2 film was formed on the Au surface *via* a surface growth mechanism. Initially, the battery was pre-discharged in a $^{18}O_2$ atmosphere, forming a $Li_2{}^{18}O_2$ film. Subsequently, switching to $^{16}O_2$ for discharge, as shown in Fig. 6b, SERS observations revealed that $Li_2{}^{16}O_2$ formed from $^{16}O_2$ gradually replaced $Li_2{}^{18}O_2$ at the Au electrode interface, indicating that the ORR occurred at the buried Au|Li_2O_2 interface.[65] In this scenario, O_2 and Li^+ can penetrate the previously deposited Li_2O_2 film, likely through grain boundaries or defect channels, reaching the underlying gold electrode surface. The transport-limiting mechanism suggests that electron transport is the primary limiting factor responsible for the sudden failure of the battery during discharge.[65] The extremely low electronic conductivity of Li_2O_2 (σ_{ea} = 2.2 × 10^{-13} S cm^{-1}) prevents efficient electron transport to the reaction interface, leading to a sharp voltage drop. Although the ionic conductivity of the Li_2O_2 film is relatively low (σ_{io} = 3.1 × 10^{-12} S cm^{-1}), experimental results indicate that Li^+ and O_2 can slowly diffuse to the interface through defect channels in the film, suggesting that ion transport is not the primary limit-

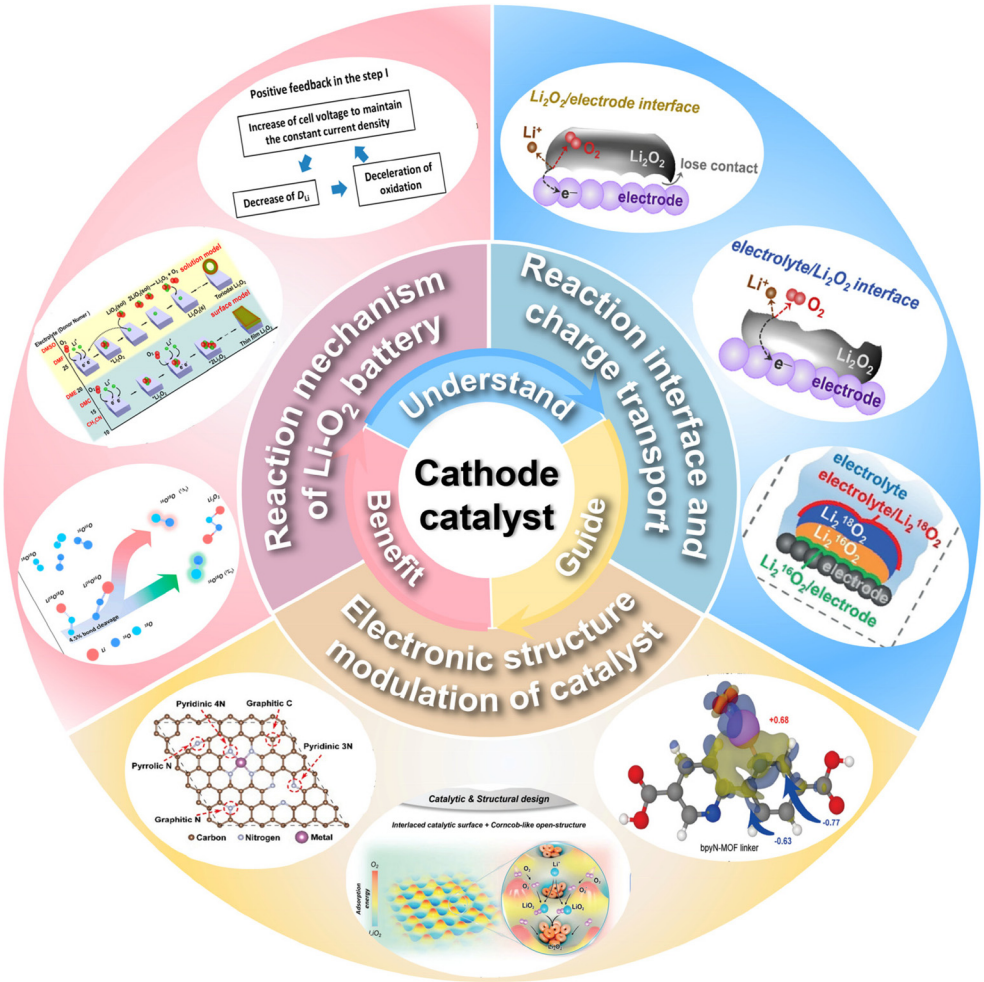

Fig. 3 A schematic illustration outlining the key topics discussed in this work, including a comprehensive analysis of the reaction mechanisms in Li–O_2 batteries,[48,49] the understanding of reaction interfaces and charge transfer mechanisms,[20,50,51] and the investigation of the electronic states of cathode catalysts.[39,52,53]

ing factor. Therefore, increasing the porosity and amorphous nature of Li_2O_2 can enhance defect density, facilitate Li^+/O_2 transport, and mitigate electron transport limitations.

During the charging process, the charge transport pathway at the electrolyte–catalyst interface is significantly influenced by the charging rate and overpotential.[69,70] At low rates and low overpotentials, the solid-solution decomposition and solvent-mediated steps during charging initiate at the Li_2O_2-electrolyte interface. Wang *et al.* revealed the oxygen release behavior of Li_2O_2 particles through isotopic tracing experiments.[48] As shown in Fig. 6c, for micron-sized particles with the outer layer of $Li_2{}^{18}O_2$ (in contact with the electrolyte) and the inner layer of $Li_2{}^{16}O_2$ (in contact with the electrode), OEMS monitoring during charging reveals that $^{18}O_2$ is released first (accounting for the first quarter of the total charge capacity), followed by $^{16}O_2$ becoming dominant. This indicates that oxygen loss originates at the Li_2O_2/electrolyte interface rather than the Li_2O_2/electrode interface. A comparison between the pure carbon electrode (VC) and the ruthenium/carbon catalyst electrode (Ru/VC) reveals that both electrodes follow the same oxygen release sequence. However, the Ru/VC electrode exhibits a reduction in charging overpotential by approximately 500 mV. This difference is attributed to the Ru catalyst, which stabilizes lithium-deficient phases on the Li_2O_2 surface (*e.g.*, $Li_{2-x}O_2$-Ru) through interfacial chemical adsorption, maintaining contact, facilitating charge transfer, and enhancing reaction kinetics. If O_2 primarily evolves at the Li_2O_2-electrolyte interface, electrons and ions must penetrate Li_2O_2 during charging, despite Li_2O_2 being a well-known wide-bandgap insulator. In fact, numerous studies have demonstrated that Li^+ vacancies and hole polarons are the primary charge carriers in Li_2O_2.[67,70,71] Perfectly ordered Li_2O_2 is a wide-bandgap insulator, with an HSE-calculated bandgap of 4.2 eV. However, under non-stoichiometric conditions or in the presence of defect states (*e.g.*, lithium vacancies), polaron conduction pathways can be activated. In Li_2O_2, hole polarons exhibit an in-plane migration barrier of only 68 meV, significantly lower than the interlayer hopping barrier.[72] This suggests that controlling

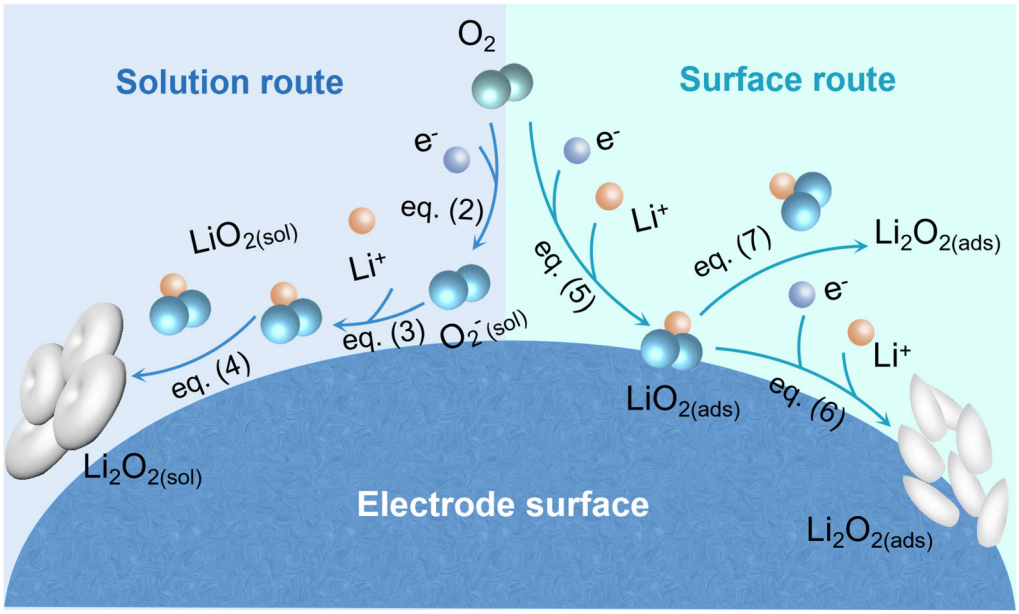

Fig. 4 Oxygen reduction mechanistic pathways in nonaqueous Li–O_2 batteries.

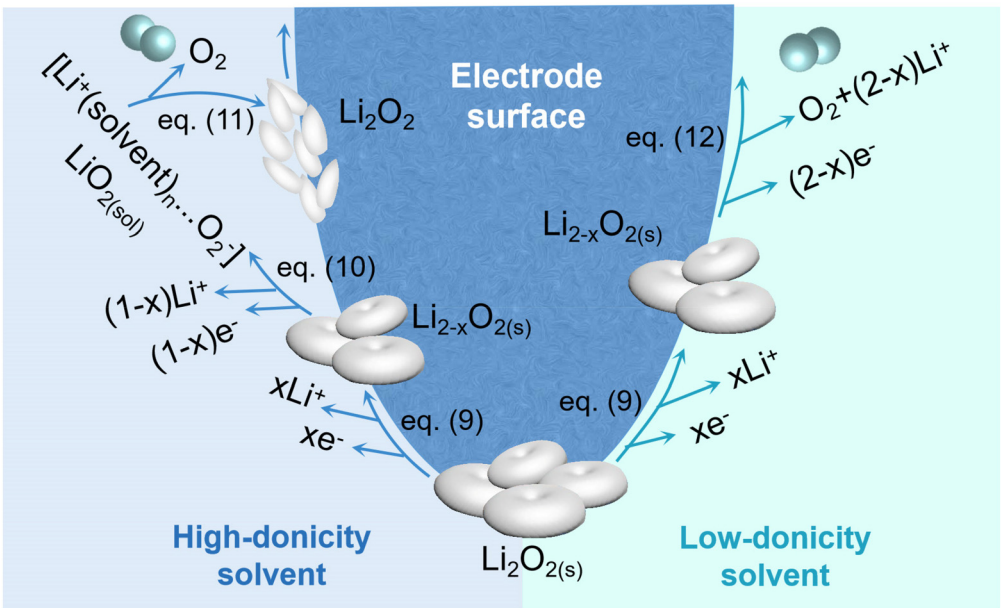

Fig. 5 Oxygen evolution mechanistic pathways in nonaqueous Li–O_2 batteries.

crystal orientation can optimize charge transport efficiency, providing valuable insights for electrode material design, such as tuning exposed crystal facets. Ball milling introduces grain boundaries and dislocation defects, increasing the overall conductivity of Li_2O_2 by approximately two orders of magnitude, from 3.4×10^{-13} S cm^{-1} to 1.1×10^{-10} S cm^{-1} at room temperature. Additionally, it generates a high-mobility Li^+ "spin reservoir", significantly enhancing ionic transport kinetics.[73] Amorphous Li_2O_2 exhibits unique transport properties due to its disordered structure. Its ionic conductivity (2×10^{-7} S cm^{-1}) is 12 orders of magnitude higher than that of its crystalline counterpart, effectively mitigating lithium-ion transport limitations during charge–discharge cycles in Li–O_2 batteries.[69] By optimizing electrode design (*e.g.*, incorporating a porous structure), the synergy between the high ionic conductivity of the amorphous phase and rapid O_2 diffusion channels can alleviate electron transport bottlenecks and extend the activity of the reaction interface. Koffi *et al.* proposed that transition metals and their oxides can act as reaction promoters by chemically converting Li_2O_2 into lithium metal oxides, which

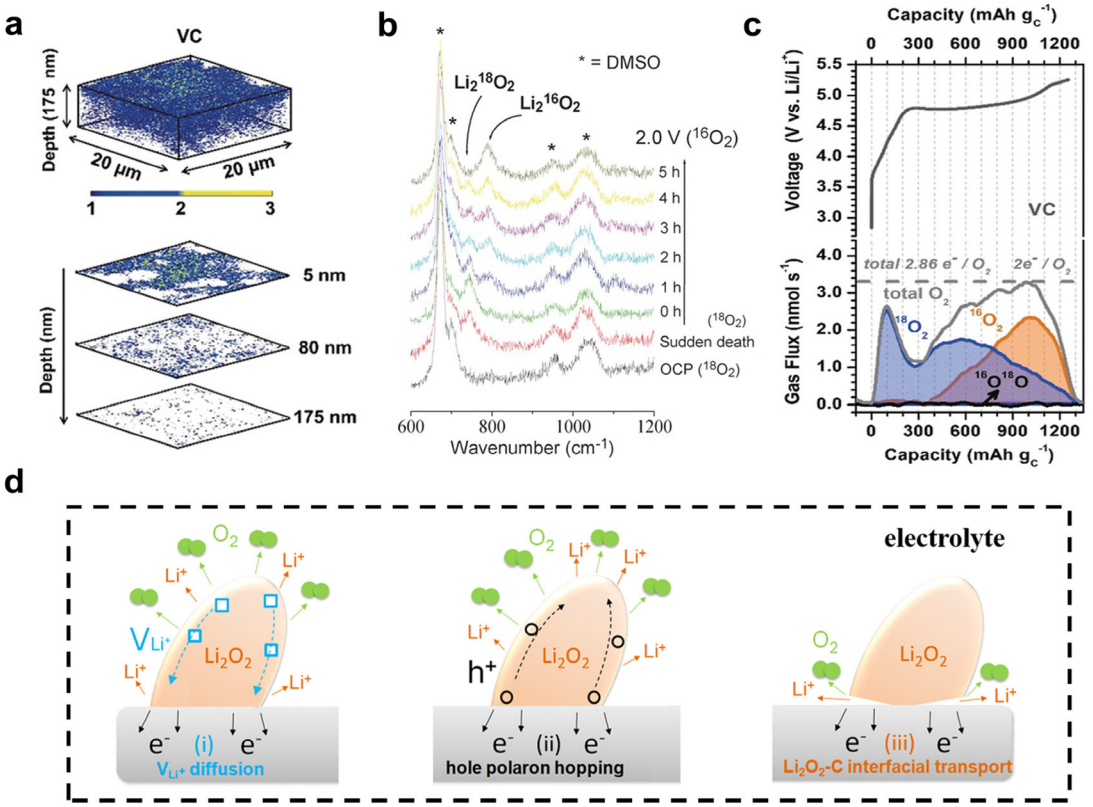

Fig. 6 (a) 3D distribution of ^{18}O in discharge products reconstructed from ToF-SIMS depth profiling, with three selected depth layers.[48] (b) *In situ* SERS collected at open circuit potential (OCP, black) and at the end of discharge under a $^{18}O_2$ atmosphere (red), followed by spectra recorded during discharge in a $^{16}O_2$ atmosphere at 2.0 V *vs.* Li/Li$^+$ over 0–5 hours.[65] (c) Charging curves of a Li–O_2 battery using a VC electrode, along with OEMS analysis of oxygen evolution.[48] (d) Schematic illustration of charge transfer during Li_2O_2 decomposition in the charging process. Decomposition occurs at the Li_2O_2-electrolyte interface, where charge transfer is mediated by (i) Li$^+$ vacancy diffusion and (ii) hole polaron hopping; (iii) reactions take place at the Li_2O_2-cathode interface.[68]

subsequently facilitate oxygen release *via* an electrochemical delithiation process.[74]

In summary, defect engineering, including grain boundary modulation, amorphization, and nanostructuring of Li_2O_2, can alleviate charge transport limitations during the charge–discharge cycles of Li–O_2 batteries.[75–77] At low charging rates, the decomposition of Li_2O_2 can be sustained through bulk and surface Li$^+$ vacancy diffusion (Fig. 6d(i)) as well as hole polaron migration (Fig. 6d(ii)). However, when the transport rate fails to keep up with the charging current, at high charging rates or high potentials, the formation of a thick Li_2O_2 film impedes charge transport, shifting the reaction site to the Li_2O_2-cathode interface (Fig. 6d(iii)).[68] Nevertheless, the stepwise decomposition at the interface can cause the structural collapse of Li_2O_2 particles from the base, leading to void formation. Detached Li_2O_2 loses electrical contact, preventing its participation in subsequent reactions and accelerating capacity degradation.[78] Therefore, enhancing the adhesion between Li_2O_2 and the cathode or designing hierarchical porous electrodes, where micropores trap reaction products and nanopores limit particle detachment, can mitigate electrochemical detachment and improve cycling performance. Notably, although the formation of a dense Li_2O_2 film restricts bulk transport, it helps maintain local electrical contact, highlighting the need for morphology control to balance transport properties and interfacial stability. Highly active solid-state catalysts (*e.g.*, Ru) enhance charge transport by forming metal oxide interfaces and stabilize Li_2O_2 intermediates through direct solid–solid interactions, thereby lowering the lithium extraction energy barrier and reducing overpotential.[79] On one hand, the coupling interaction between the electrode surface and Li_2O_2 can regulate the interfacial delithiation process. On the other hand, this necessitates that the substrate material exhibits strong resistance to Li_2O_2 oxidation. The oxidation tendency or multivalent capability of the catalyst determines its ability to stabilize Li_2O_2 intermediates, thereby influencing OER activity.[74] The position of the catalyst's d-band center directly influences the adsorption strength and decomposition pathway of Li_2O_2. Interfacial hybridization can create delocalized electronic channels, leading to charge redistribution. Qian *et al.* designed a nickel-based catalyst encapsulated in carbon nanotubes (CNTs), denoted as Ni/Ni_3C-CNT.[66] The electron delocalization of the inner Ni/Ni_3C material induces interfacial charge interactions, redistributing the electron density and surface electrostatic potential of the outer carbon shell. This modulation of surface adsorption states governs the kine-

tics of Li–O_2 chemistry. The Ni/Ni_3C-CNT catalyst exhibits moderate adsorption strength toward superoxide intermediates, effectively lowering the reaction energy barrier and achieving remarkable rate performance.

2.3 Rational design of cathode catalysts

In Li–O_2 batteries, the precise tuning of the cathode catalyst's electronic structure directly determines catalytic activity and reaction kinetics.[80,81] The position of the d-band center in transition metal catalysts significantly influences the reaction energy barrier by modulating the adsorption free energy of reaction intermediates (*e.g.*, O_2^-, LiO_2, Li_2O_2). Guo *et al.* employed a high-entropy strategy to design a series of alloy catalysts with widely distributed d-band centers.[116] Their study revealed that catalytic activity follows a volcano-shaped curve as a function of adsorption strength, adhering to the Sabatier principle of heterogeneous catalysis. It was demonstrated that an excessively high d-band center leads to overly strong interactions between the catalyst and intermediate species, resulting in slow desorption kinetics and an increased reaction energy barrier. Conversely, an extremely low d-band center provides insufficient binding strength, causing product loss and surface passivation. As a demonstration of the trade-off between adsorption and desorption strength, HEA-PtIr exhibited the highest catalytic activity in Li–O_2 batteries, displaying an optimal adsorption capability. Additionally, a high surface electron density enhances the accessibility of active sites, facilitating oxygen molecule adsorption and dissociation. Intrinsic defects in catalysts, such as non-metal and metal vacancies, can introduce unsaturated coordination sites, enhance electronic conductivity, and lower reaction energy barriers. Heteroatom doping can modulate local electron density through orbital hybridization. For example, Co_3O_4 with a higher concentration of surface oxygen vacancies promotes the formation of Li_2O_2 morphologies that are more easily decomposable during charging, thereby enhancing battery reversibility and cycling stability.[82] A cation vacancy-rich composite, VCo-$CoSe_2$@MXene, exhibited enhanced covalency upon Co vacancy introduction, facilitating electron transfer from Ti_3C_2 MXene to $CoSe_2$ and optimizing the electronic structure of interfacial Co sites.[83] Notably, the secondary Co site adjacent to the Co vacancy served as an active center for the oxygen reduction reaction, leading to a low overpotential (0.35 V) and excellent cycling stability (250 cycles at 500 mA g^{-1}) in Li–O_2 batteries. Heteroatoms, such as metal dopants, also serve as an effective strategy for modulating local electron density. Loading various metal elements onto Co_3O_4 hollow spheres to substitute Co^{3+} centers in the octahedral structure establishes electron transfer pathways that stabilize Co^{3+} centers during charge–discharge cycles.[84] This strategy maximizes the number of available active sites, facilitates oxygen adsorption and Li_2O_2 nucleation, and spatially separates active Co^{3+} centers, directing the growth of well-dispersed Li_2O_2 nanosheets.

The design of the air cathode directly influences charge transfer efficiency at the electrolyte/catalyst interface, thereby determining overall battery performance.[85,86] First, the air cathode must exhibit high electrical conductivity. The deposition of Li_2O_2 can lead to electrode surface passivation. At low overpotentials, electrons must transfer from the insoluble Li_2O_2 to the cathode surface, necessitating a cathode material with high electronic conductivity. Studies have shown that integrating catalysts with conductive materials (*e.g.*, carbon nanotubes,[87] graphene[88]) can significantly enhance cathode conductivity and improve charge–discharge performance. Catalytic activity is a key performance metric for the air cathode. The cathode catalyst must effectively catalyze the ORR and OER reactions to reduce overpotential and enhance battery energy efficiency.[89,90] The electronic structure of the catalyst, particularly the electron density of the metal d-band, surface electron density, and adsorption capacity for intermediates, directly influences catalytic performance. Proper tuning of the d-band center can optimize the catalyst's adsorption energy for reaction intermediates, thereby enhancing catalytic activity. Additionally, defects and doped sites on the catalyst surface can increase the number of active sites, further facilitating electrochemical reactions.[91] Furthermore, the air cathode must exhibit high chemical stability. During long-term battery operation, the formation and decomposition of Li_2O_2 is a recurring process, requiring the catalyst to maintain structural and functional stability. Side reactions, such as the formation of LiOH and Li_2CO_3, may block cathode pores, hindering long-term battery performance. Therefore, air cathode materials should possess strong corrosion resistance and durability to suppress side reactions and ensure the long-term stability of catalytic active sites. Structurally, the air cathode should have a high porosity to provide sufficient space for oxygen adsorption and Li_2O_2 deposition.[92] Studies have shown that mesoporous and microporous structures facilitate efficient Li_2O_2 storage and gas diffusion, thereby improving discharge capacity and rate performance.

3. Modulating cathode catalyst electronic properties

In Li–O_2 batteries, the electronic structure of the cathode catalyst plays a decisive role in the adsorption/desorption behavior of reaction intermediate, charge transfer efficiency, as well as the reaction pathways, energy barriers, and overall performance of the ORR and OER.[93–95] In recent years, with advancements in DFT calculations and *in situ* characterization techniques, researchers have gradually unveiled the structure–activity relationships between catalyst electronic properties and catalytic activity. This has led to the development of a multiscale design approach guided by electronic regulation. Therefore, this paper systematically reviews the current primary strategies for optimizing electronic structures, including the modulation of the metal d-band center, optimization of non-metallic p-orbital sites, e_g orbital occupancy, orbital hybridization, facet-directed exposure, and innovative strategies assisted by external fields. It also explores their role and potential in enhancing the electrochemical performance of Li–

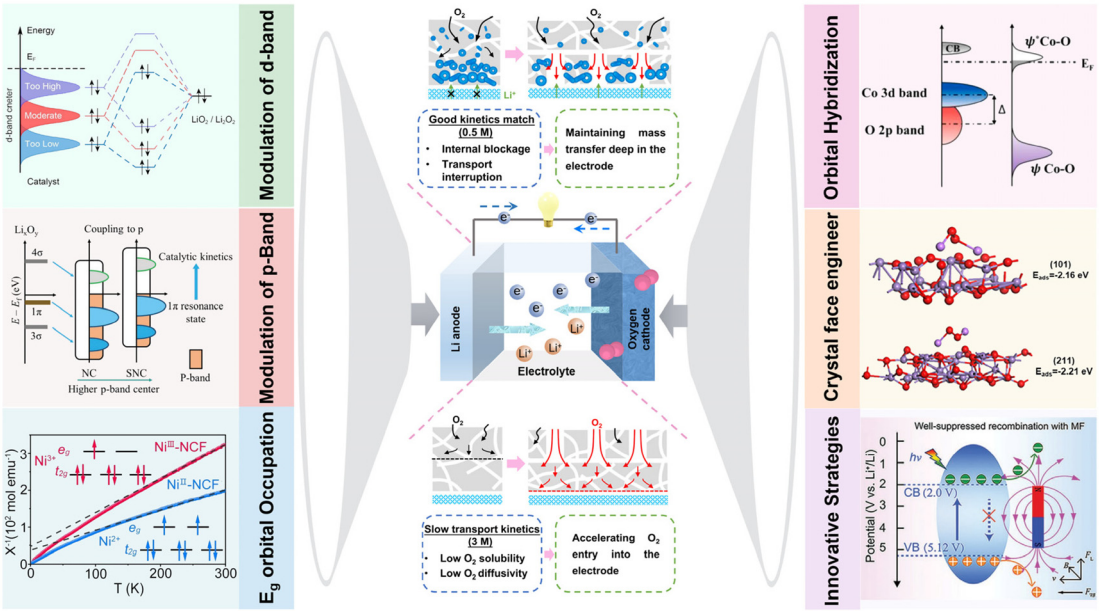

Fig. 7 This work discusses strategies for modulating the electronic properties of catalysts, including modulation the metal d-band center,[116] non-metallic p-orbital sites,[117] e_g orbital occupation,[106] orbital hybridization,[118] optimization of exposed crystal facets,[119] and innovative approaches assisted by external fields.[120]

O_2 batteries (Fig. 7). Table 1 provides a summary of key parameters for several representative cathode catalysts in Li–O_2 batteries reported over the past three years, including categories, electrolytes used, overpotential, discharge capacity, and cycle life, for readers to gain a comprehensive understanding. This review aims to deepen the understanding of catalytic mechanisms and provide theoretical and practical guidance for the rational design of high performance cathode catalysts.[52,66,83,84,96–115]

3.1 Modulation of the d-band center

Research on the regulation of catalyst electronic structures, particularly d-band center optimization, has been continuously emerging, providing a solid theoretical foundation and experimental evidence for improving the performance of Li–O_2 batteries across various material systems and design strategies.[121–125] Guo *et al.* systematically investigated the effect of d-band center position on the adsorption strength of oxygen intermediates by designing a series of alloy catalysts with a broad distribution of d-band centers (a wide range of adsorption strengths) through a high-entropy strategy.[116] The binding energies of LiO_2/Li_2O_2 with five different alloys exhibit corresponding energy conversion efficiencies, as shown in Fig. 8a and b. As the d-band center decreases in the order of HEA > PtIr > HEAPtIr > HEAIr > HEAPt, it confirms that the relationship between oxygen binding energy on the catalyst and energy conversion efficiency is not linear but follows a volcano-type trend. The peak performance is observed for HEAPtIr (d-band center = −2.64 eV), which exhibits the lowest overpotential of 0.38 V and an energy conversion efficiency exceeding 80%. The projected and integrated crystal orbital Hamilton population (pCOHP and iCOHP) values further quantitatively evaluate the interaction between O1 and O2 bonds (Fig. 8c). From HEAPt to HEAPtIr, as the binding energy increases, a greater number of antibonding states become occupied, indicating that HEAPtIr further weakens the interaction between O1 and O2 compared to HEAIr and HEAPt. Notably, the -iCOHP values of HEA and PtIr are close to zero, indicating minimal interaction between oxygen atoms. This weak interaction makes the decomposition of LiO_2 (or Li_2O_2) more challenging, ultimately affecting the kinetics of the charging process. Fig. 8d and e summarize the relationship between the d-band center of cathode catalysts and catalytic activity in LiO_2 batteries. An excessively high d-band center results in overly strong interactions with oxygen species, leading to slow desorption kinetics, which hinders subsequent reactions and deactivates active sites. Conversely, an excessively low d-band center provides insufficient binding strength, leading to product loss and sluggish charge transfer, which is detrimental to rate performance and stability. An optimal d-band center ensures appropriate adsorption strength with oxygen species, balancing adsorption and desorption, thereby achieving the ideal point in the Sabatier relationship. In the study of high-entropy perovskite oxide ($LaSr(5TM)O_3$), five transition metal elements (TM = Cr, Mn, Fe, Co, Ni) occupy the B-site metal lattice.[81] As shown in Fig. 8f, the compressive strain in $LaSr(5TM)O_3$ effectively modulates the occupancy state of the 3d orbitals at active cobalt sites (Co^{2+} → Co^{3+}). Consequently, the d-band center of Co shifts from −2.08 eV to −1.37 eV (Fig. 8g and h), enhancing the adsorption capability of LiO_2 intermediates at cobalt sites. Additionally, the high electron-withdrawing capability of Cr sites ensures sufficient

Table 1 Summary of recent progress in different cathodic catalysts and the corresponding electrochemical performance for Li–O_2 batteries

Cathode catalyst	Electrolyte	Overpotential (V)/ [current (mA g^{-1})]	Capacity (mA h g^{-1})/ [current (mA g^{-1})]	Cycles [current (mA g^{-1})]/ limited capacity (mA h g^{-1})	P.Y	Ref.
$MnCr_{0.5}Co_{1.5}O_4$	1 M LiTFSI/TEGDME	0.67/100	16 388/100	329/(200/1000)	2024	94
WCoFe@Ni	1 M LiTFSI/DMSO	1.24/200	5800/200	>400/(500/1000)	2023	95
Mo_3P@MO	—	1.05/100	4720/500	500/(500/500)	2022	96
Ni-NG SAC	1 M LiTFSI/TEGDME	—/200	24 248/200	>500/(300/1000)	2024	97
$Ti_{0.87}O_2$/MXene	—	0.69/200	13 596/100	407/(1000/600)	2024	81
SPC-2	1 M LiTFSI/TEGDME	1.04/200	20 287/200	226/(200/600)	2022	98
$CeO_{2-\delta}$	1 M LiTFSI/DMSO	1.09/250	—	>35/(250/10 000)	2023	99
GMS-sheets	1 M LiTFSI + $LiNO_3$/ TEGDME	0.82	>6200 mA h g^{-1}/0.4 mA cm^{-2}	260/(0.4 mA cm^{-2})/4 mA h cm^{-2}	2023	100
bpyN-MOF	1 M LiTFSI/TEGDME	0.487/200	17 275/100	270/(2000/1000)	2024	51
$NiCo_2O_4$@CeO_2	1 M LiTFSI/TEGDME	1.07/500	5586/500	400/(500/500)	2022	101
GMS-CP	0.5 M LiTFSI/TEGDME		6727/100	307/(0.1 mA cm^{-2}/0.25 mA h cm^{-2})	2023	102
Ir_1/Co_3O_4	—	0.305/200	16 861/200	180/(200/500)	2023	82
UIO-66-NH_2	—	0.87/100	12 261/100	169/(200/1000)	2023	103
NiIII-NCF	1 M LiTFSI/TEGDME	0.92/500	16 800/500	>200/(500/1000)	2022	104
PtAu	1 M LiTFSI/TEGDME	0.36/100	5049/100	220/(500/1000)	2022	105
Ce_1/CoO	1 M LiTFSI/TEGDME	0.46/250	37 462/250	136/(250/1000)	2024	106
FeCo-N_4/HCS	1 M LiTFSI/TEGDME	0.64/200	1637/200	275/(200/1000)	2023	102
$Ru_{0.8}Pd_{0.2}$/Fe-CNCs	1 M LiTFSI/TEGDME	0.84/100	31 211/100	300/(200/1000)	2023	107
Ni/Ni_3C-CNT	1 M LiTFSI/25% EMIM-BF_4 + 75% DMSO	0.43/200	21 612/0.5 mA cm^{-2}	170/(0.5 mA cm^{-2}/0.5 mA h cm^{-2})	2022	65
NiRu-HTP	—	0.76/200	18 280/500	>200/(500/1000)	2022	108
Na–Pb-MOF	—	0.52/100	6247/100	140/(100/1000)	2023	109
TA-ZIF@Ru-280	1 M LiTFSI/TEGDME		7000/200	300/(200/500)	2023	110
$NiCO_2O_4/MnO_2$	1 M LiTFSI/TEGDME	0.73/0.5 mA cm^{-2}	7000/0.2 mA cm^{-2}	800/(0.2 mA cm^{-2}/0.5 mA h cm^{-2})	2024	111
Pd_3Pd	1 M LiTFSI/TEGDME	0.45/100	7746/—	175/(500/1000)	2023	112

electron exchange, further strengthening the adsorption of LiO_2. The charge–discharge overpotential is reduced to 0.79 V, extending the cycle life to 226 cycles.

By employing a heteroatomic doping strategy, such as Ni-doped RuO_2 catalysts (Ni-RuO_2), electron redistribution effectively lowers the d-band center of RuO_2, thereby weakening the adsorption strength of oxygen intermediates.[126] The Ni-RuO_2 catalyst exhibits a low overpotential of 0.79 V and an extended cycle life exceeding 791 cycles. Additionally, non-metal doping effectively induces electron delocalization, leading to changes in the d-band center at metal sites. As illustrated in Fig. 9a, moderate N doping in Ni_5P_4 (N-Ni_5P_4/5N-Ni_5P_4) induces a downward shift in the d-band center, whereas higher doping levels (10N/15N-Ni_5P_4) lead to an upward shift. This suggests that appropriate doping can optimize the adsorption/desorption equilibrium of oxygen intermediates during the redox cycle. As the d-band center shifts downward, the antibonding states induced by O 2p–Ni 3d coupling move further away from the Fermi level, weakening the interaction between intermediates and the catalyst surface. Meanwhile, the significant contribution of P 2p orbitals to the TDOS near the Fermi level (Fig. 9b) ensures that the system retains high conductivity after oxygen intermediate adsorption, facilitating the growth of discharge products. Theoretical calculations indicate that a downward shift in the d-band center enhances antibonding orbital electron occupancy (Fig. 9c), thereby reducing the dissociation energy barrier of oxygen species, providing a key descriptor for catalyst design.[127] A novel bimetallic conductive metal–organic framework (MOF) catalyst, NiRu-HTP, significantly enhances the oxygen reduction/evolution reaction (ORR/OER) kinetics in Li–O_2 batteries by synergistically tuning the d-band center and interfacial orbital hybridization.[111] As shown in Fig. 9d and e, the d-band centers of Ni-HTP and NiRu-HTP are −1.82 eV and −1.43 eV, respectively. The upward shift of the d-band center in NiRu-HTP enhances its interaction with O_2 molecules. DFT calculations indicate that at the Ni–N_4 site, the d_{xz} and d_{yz} orbitals of Ni overlap with the π orbitals of O_2, forming (d_{xz}/d_{yz}–π)* orbitals (Fig. 9f). At the Ru–N_4 site, the d_{z^2} and d_{xz} orbitals of Ru couple with the σ and π orbitals of O_2, forming (d_{z^2}–σ)* and (d_{xz}–π)* orbitals, respectively (Fig. 9g). In NiRu-HTP, the (d_{z^2}–σ)* and (d_{xz}–π)* orbitals exhibit lower electron occupancy and higher energy levels, indicating enhanced adsorption of O_2. As shown in Fig. 9h and i, differential charge density maps further confirm that O_2 adsorption energy on NiRu-HTP (−1.47 eV) is significantly higher than that on Ni-HTP (0.28 eV). Additionally, NiRu-HTP transfers more electrons to O_2 (0.47 e^- compared to 0.22 e^-), indicating more effective O_2 activation. By tuning the d-band center to regulate the oxygen reduction and evolution reaction pathways, the NiRu-HTP cathode significantly reduces charge–discharge polarization to 0.76 V and maintains stable performance over 200 cycles without significant degradation.

Through heterointerface engineering,[103,129,130] as demonstrated in the Co_3O_4@$NiFe_2O_4$ composite catalyst (Fig. 9j and k), the introduction of a heterogeneous interface can modulate the occupancy state of d orbitals at active metal sites *via* elec-

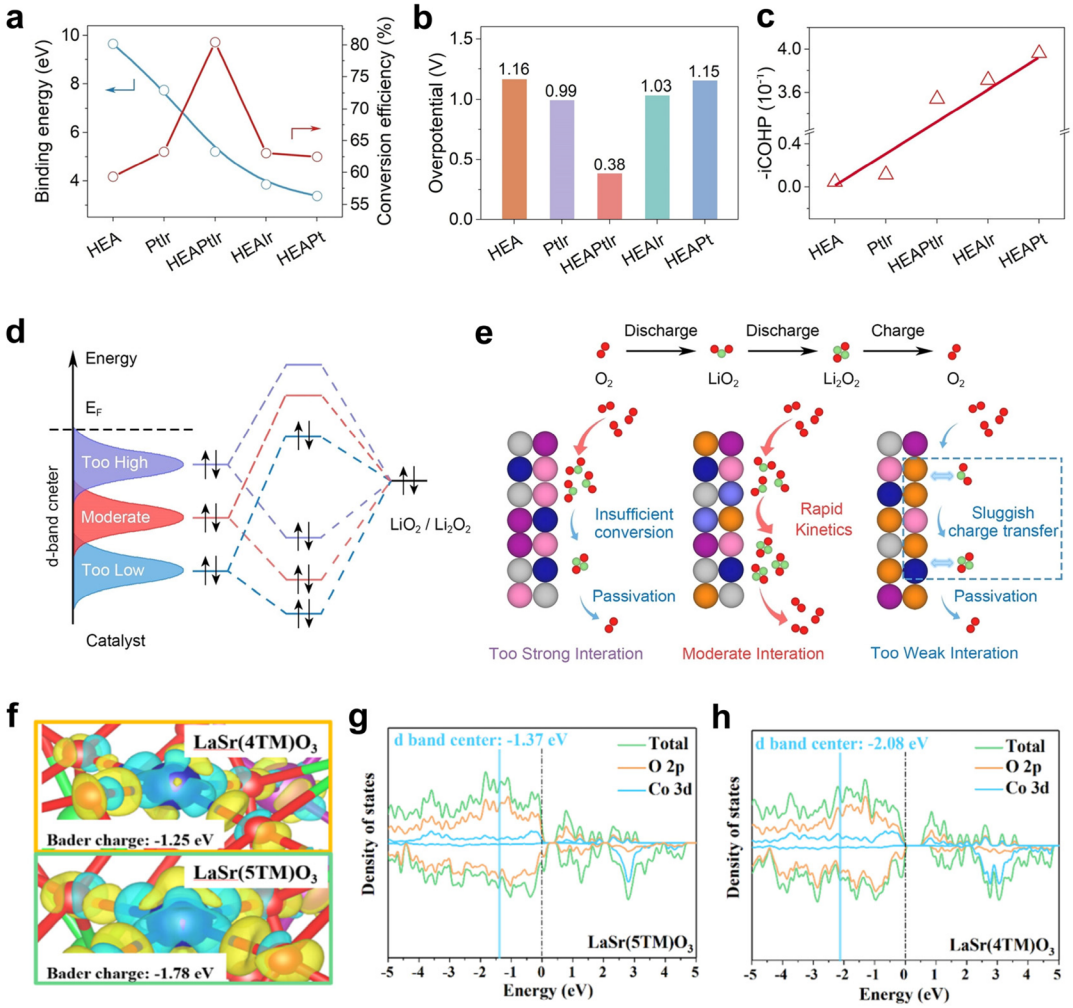

Fig. 8 (a) Binding energy of LiO_2 with cathode catalysts (HEA, PtIr, HEAPtIr, HEAIr, HEAPt) and the corresponding energy conversion efficiency. (b) Overpotentials of different alloy catalysts at a current density of 500 mA h g^{-1}. (c) -iCOHP values of the corresponding systems. (d) Orbital interactions between different d-band center catalysts and LiO_2/Li_2O_2. (e) Corresponding catalytic effects.[116] (f) Charge density differences at Co sites in $LaSr(5TM)O_3$ and $LaSr(4TM)O_3$ (yellow regions represent charge accumulation, and blue regions represent charge depletion). PDOS and DOS of (g) $LaSr(5TM)O_3$ and (h) $LaSr(4TM)O_3$.[81]

tron redistribution, leading to an upward shift of the d-band center.[128] This enhances oxygen intermediate adsorption and reaction kinetics (Fig. 9l). Additionally, high-entropy alloy (HEA) heterostructures (HEA@Pt) optimize the d-band center position of catalysts through the synergistic effects of multiple metal components and interfacial electron redistribution.[131] Single-atom catalysts also exhibit significant advantages in d-band center modulation.[53,84,132,133] A single-atom Ir catalyst (Ir@CeO_2) supported on the (111) facet of CeO_2 leverages the electronic buffering effect of CeO_2, which shifts the d-band center of Ir sites closer to the Fermi level.[133] This enhances Lewis acidity and effectively optimizes the adsorption of LiO_2 intermediates.

In recent years, significant progress has been made in optimizing the reaction kinetics of Li–O_2 batteries by tuning the d-band center of catalysts.[111,116,134,135] Studies have shown that the position of the d-band center directly determines the adsorption strength of oxygen intermediates (LiO_2, Li_2O_2), thereby influencing the energy barriers and cycling stability of the ORR/OER. Strategies such as high-entropy alloy design, heteroatomic doping, interface engineering, and single-atom catalysis achieve precise modulation of the d-band center at active sites through electronic structure rearrangement (*e.g.*, orbital hybridization, charge transfer, and strain effects). These approaches enable a balance between the adsorption and dissociation kinetics of oxygen intermediates, significantly reducing charge–discharge polarization and extending cycle life, thereby elucidating the complexity and feasibility of d-band center regulation.[66,136,137]

3.2 Modulation of p-band non-metallic center

Research on optimizing p-band non-metallic sites primarily focuses on modifying non-metallic sites, such as nitrogen doping,[138,139] phosphorization,[100,117] sulfidation,[113] and non-

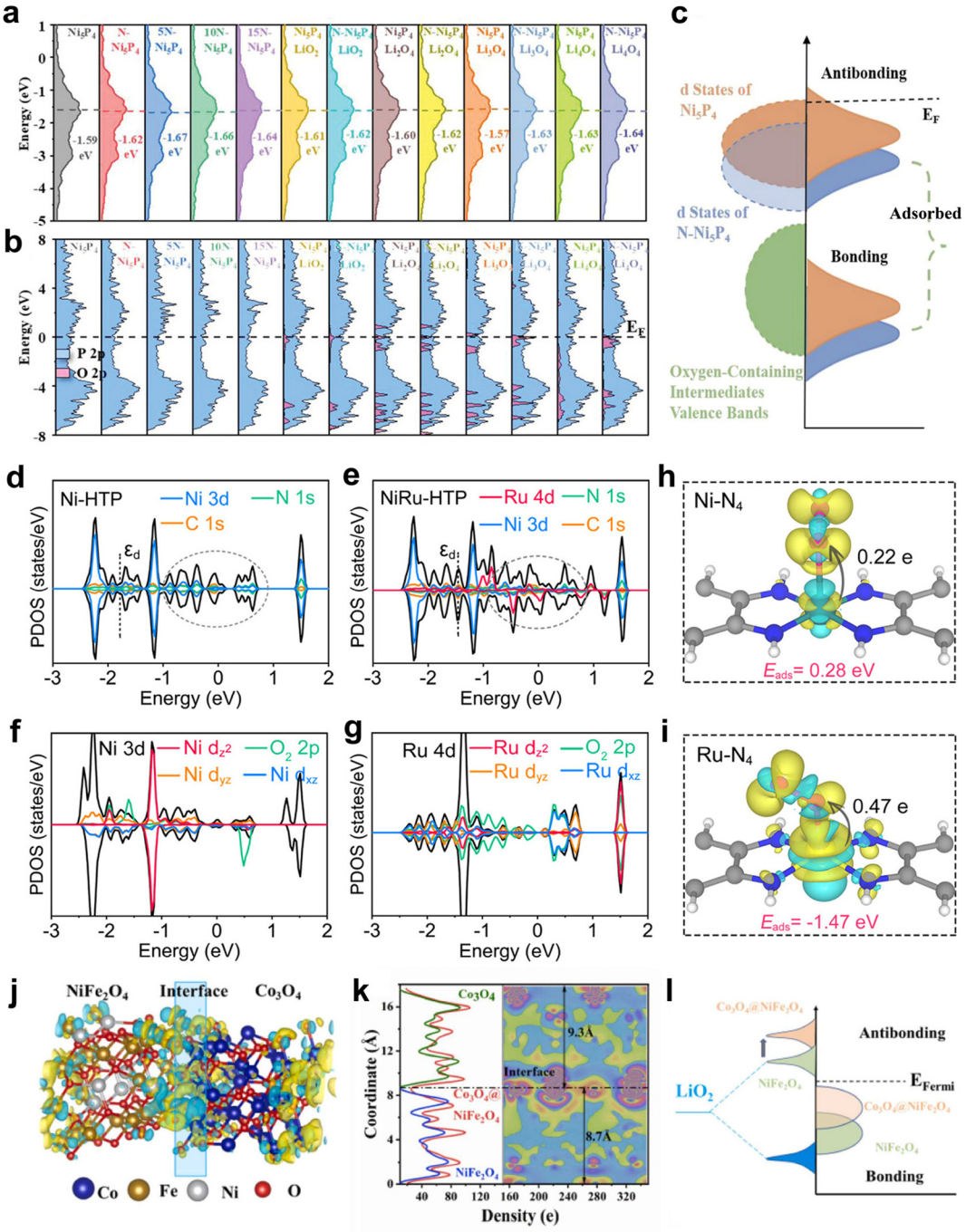

Fig. 9 (a) d orbits PDOS of Ni_5P_4 with different levels of N doping and after adsorption of oxygen-containing intermediates. (b) P 2p and O 2p orbital distributions before and after adsorption of oxygen-containing intermediates on Ni_5P_4 and N-Ni_5P_4. (c) Schematic diagram of bonding interactions between the valence band of surface adsorbates and the metal d-band.[127] TDOS and PDOS of Ni 3d and O 2p orbitals in (d) NiN_4-O_2 within Ni-HTP and (e) Ru N_4–O_2 within NiRu-HTP. PDOS distribution of (f) Ni 3d orbitals and (g) O 2p orbitals corresponding to (d) and (e). Differential charge density of (h) Ni-HTP and (i) NiRu-HTP after O_2 adsorption, where cyan and yellow regions indicate charge depletion and accumulation, respectively.[111] (j) Differential charge density map of Co_3O_4@$NiFe_2O_4$. (k) Planar-averaged charge density difference (CDD) distribution on the surfaces of Co_3O_4, $NiFe_2O_4$, and Co_3O_4@$NiFe_2O_4$ (right); numerical values on the left indicate specific surface charge densities of each material. (l) Schematic diagram of valence band interactions between adsorbed LiO_2 and the Ni 3d orbitals on $NiFe_2O_4$ and Co_3O_4@$NiFe_2O_4$ surfaces.[128]

metal vacancy introduction,[113,140] to enhance the electronic structure and reaction kinetics of catalysts. For instance, non-metal doping reconstructs the electronic structure of carbon-based catalysts. Surface phosphorization of sawdust-derived carbon catalysts (Fig. 10a) effectively mitigates the corrosion between carbon materials and the electrolyte/products.[100] As shown in Fig. 10b, the SPC cathode features an open and orderly microchannel structure, providing efficient mass trans-

fer pathways, Li_2O_2 storage space, and a highly active three-phase interface during the charge–discharge process in Li–O_2 batteries. As illustrated in Fig. 10c–e, the doped P atoms preferentially substitute one N atom in pyrrolic-N sites, forming graphitized P–N active sites that act as reaction kinetics promoters. Compared to untreated carbon electrodes, SPC electrodes accelerate reaction kinetics through high O_2/LiO_2 adsorption energies (O_2: −1.15 eV, LiO_2: −2.03 eV) and enhanced conductivity. Even under long-term cycling in the presence of highly oxidative discharge products ($Li_{2-x}O_2$), SPC effectively suppresses byproduct formation and corrosion of sawdust-derived carbon catalysts. Further studies reveal that introducing sulfur anions into nitrogen–carbon catalysts (SNC) forms N–S pairs, effectively tuning the p-band center of pyridinic nitrogen groups. This accelerates the formation and decomposition of $Li_{1-3}O_2$ intermediates, reducing the battery overpotential to 0.35 V.[117]

Oxygen vacancies, as key regulators of catalyst electronic structures, exhibit significant interfacial reaction optimization effects in Li–O_2 batteries. Studies indicate that precisely controlling the concentration of oxygen vacancies can effectively direct the nucleation and decomposition pathways of Li_2O_2.[3,82,142,143] In cobalt oxide-based studies, Co_3O_4 nanoboxes with varying surface oxygen vacancy concentrations were synthesized as cathode materials for Li–O_2 batteries by controlling catalyst particle size.[82] Fig. 10f a_{1-3} and b_{1-3} depict the electrode surfaces of the samples in their initial state, after full discharge, and after charging, respectively. After discharge, small-sized S-Co_3O_4, due to its high specific surface area and abundant oxygen vacancies, induces the uniform deposition of Li_2O_2 in a thin-film morphology with smaller and evenly distributed particles. In contrast, large-sized B-Co_3O_4, with insufficient oxygen vacancies, results in the aggregation of Li_2O_2 into micron-sized clusters (~4 μm). The surface of S-Co_3O_4 contains more oxygen vacancies, providing additional nucleation sites for Li_2O_2. This facilitates the formation of highly dispersed and smaller-sized Li_2O_2, ensuring better contact with the catalyst surface. During subsequent charging, the efficient transport of Li^+ and electrons at the interface facilitates the rapid decomposition of Li_2O_2, enhancing the battery's reversibility and cycling stability. However, Li_2O_2 catalyzed by B-Co_3O_4 continues to migrate and aggregate on the catalyst surface, forming larger particles that reduce decomposition efficiency during charging. As cycling progresses, Li_2O_2 continuously accumulates (Fig. 10g). This provides valuable insights into the structural design of cathode catalysts and the regulation of Li_2O_2 morphology in Li–O_2 batteries. The hollow catalyst TA-ZIF@Ru-280, synthesized *via* chemical etching, significantly enhances electron transport capability and reaction kinetics by optimizing active sites and oxygen vacancy distribution.[113] Similarly, CuS_{1-x} nanoflowers, designed and synthesized based on a defect engineering strategy, serve as cathode catalysts for Li–O_2 batteries, effectively optimizing reaction kinetics.[141] Sulfur vacancies induce changes in the valence state distribution of Cu and trigger charge redistribution (Fig. 10h). This shifts the Fermi level of CuS_{1-x} toward the conduction band, significantly enhancing its electronic conductivity (Fig. 10i). Additionally, sulfur vacancies create electron-deficient regions, providing unsaturated Cu active sites that facilitate stable LiO_2 adsorption. This promotes the formation of highly conductive LiO_2 intermediates *via* surface pathways, thereby lowering the decomposition energy barrier of Li_2O_2 (Fig. 10j). This modification not only enhances the electronic conductivity of the catalyst but also strengthens charge transfer at Cu active sites, improving the adsorption stability of intermediate species.

3.3 e_g orbital occupation

The occupancy of the e_g orbitals serves as a key descriptor for the electronic structure of transition metal ion d-orbitals, directly influencing the adsorption–desorption equilibrium between catalyst surfaces and reaction intermediates.[106,144,145] According to molecular orbital theory, tuning the e_g orbital occupancy modulates the filling degree of antibonding orbitals (σ and π), thereby adjusting the adsorption energy of intermediates such as $*O_2^-$, $*LiO_2$, and $*Li_2O_2$. The design of an ideal catalyst requires precise regulation of electron distribution within an optimal e_g orbital occupancy range to balance adsorption and desorption, ultimately achieving high-performance ORR and OER activities.

The introduction of highly electronegative metal elements (*e.g.*, Mo or Au) effectively modulates the e_g orbital occupancy of neighboring metal atoms. For example, in the PtAu alloy, the highly electronegative Au captures more eg electrons from Pt, resulting in Pt atoms in PtAu having fewer e_g electrons compared to those in PtRu.[107] As shown in Fig. 11a, the Pt 4f peak of PtAu exhibits a noticeable blue shift relative to that of PtRu. PDOS calculations reveal that the number of e_g electrons on the Pt 5d orbitals in PtAu is 2.84, lower than the 2.96 in PtRu (Fig. 11b). The reduced e_g occupancy of Pt in the PtAu alloy leads to an upward shift of the Pt d-band, significantly decreasing antibonding electrons and thereby enhancing the adsorption strength between LiO_2 and PtAu. Consequently, during the decomposition of Li_2O_2, PtAu exhibits a lower energy barrier (0.842 eV) compared to PtRu (1.01 eV) (Fig. 11c). Specifically, in the oxygen reduction reaction ORR process, the PtRu catalyst exhibits weak affinity toward LiO_2, leading to the formation of ring-shaped Li_2O_2 *via* a solution-growth model. The insufficient Li_2O_2/cathode interface results in sluggish OER kinetics and undesired side reactions. In contrast, the strong interaction between LiO_2 and the PtAu cathode facilitates the deposition of Li_2O_2 nanosheets on the PtAu electrode surface *via* a surface-growth model. Benefiting from the superior contact interface between Li_2O_2 nanosheets and the PtAu electrode, PtAu demonstrates a lower OER energy barrier and outstanding catalytic activity. Consequently, Li–O_2 batteries based on the PtAu cathode exhibit a low charge overpotential of 0.36 V and excellent cycling stability over 220 cycles (with a capacity limit of 1000 mA h g^{-1}), ranking among the best-performing noble metal-based cathodes reported to date.

Spin-state modulation alters the electron distribution of transition metal ions, thereby influencing the occupancy of

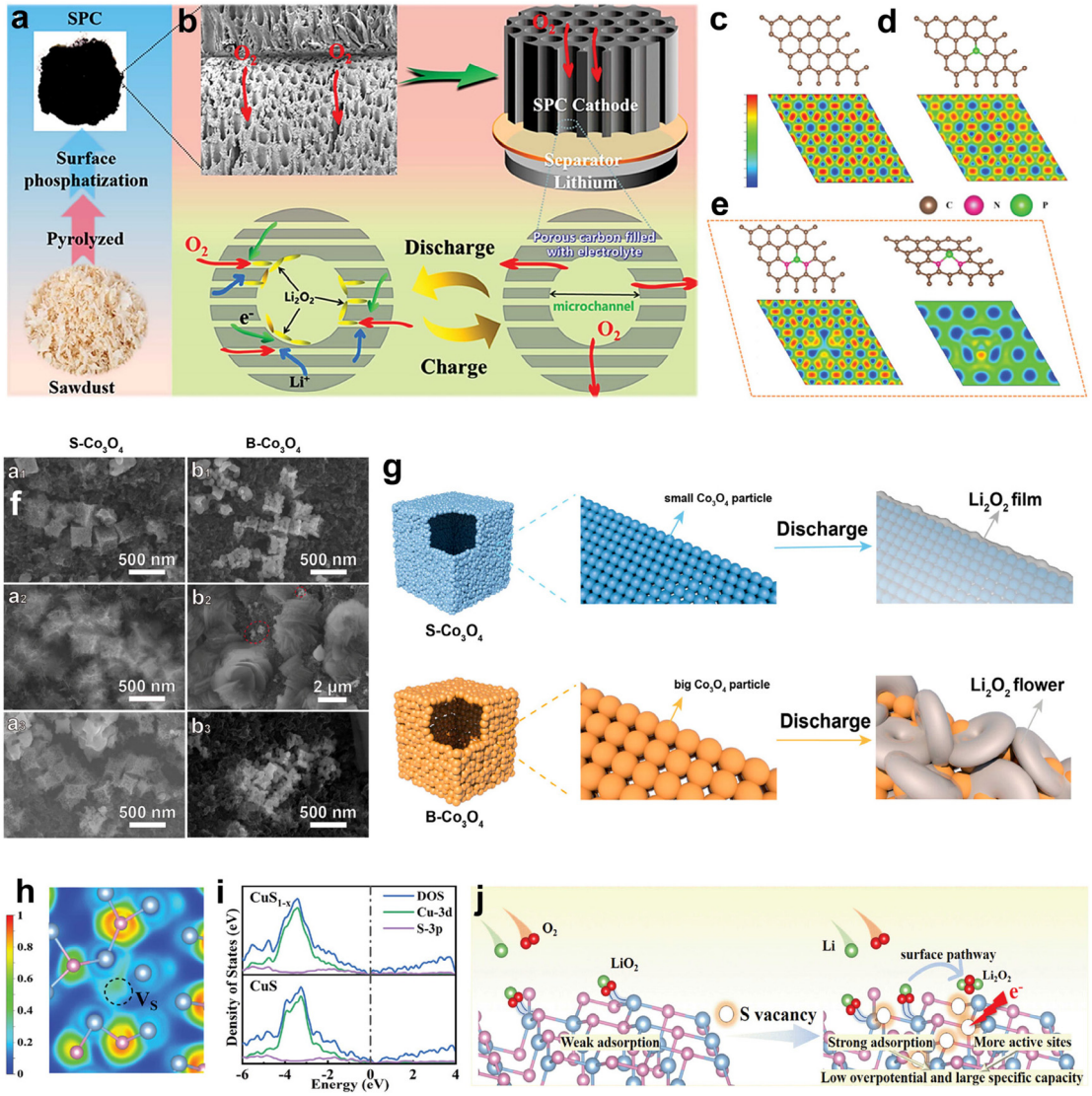

Fig. 10 (a) Schematic illustration of SPC catalyst synthesis. (b) Schematic diagram of a Li–O_2 battery using an SPC cathode. The SPC cathode features an open and orderly arranged microchannel structure, facilitating Li^+ transport and oxygen diffusion. (c) Electronic structure of carbon and ELF. ELF of graphitized (d) P–C sites and (e) P–N sites.[100] (f) *Ex* situ SEM images of (a_1–a_3) S-Co_3O_4 and (b_1–b_3) B-Co_3O_4 cathodes at different stages: (a_1 and b_1) initial state; (a_2 and b_2) fully discharged state; (a_3 and b_3) fully charged state. (g) Schematic illustration of the Li_2O_2 formation mechanism on S-Co_3O_4 and B-Co_3O_4 surfaces.[82] (h) ELF of CuS_{1-x}. (i) TDOS of CuS and CuS_{1-x}. (j) Schematic illustration of the mechanism by which CuS_{1-x} catalyst enables high-performance catalysis.[141]

the e_g orbitals.[147–149] In two-dimensional MOFs, oxidative treatment of NiII-NCF nanowire arrays adjusts the spin state of some Ni^{2+} metal centers ($t_{2g}^6e_g^2$) to a higher valence state, Ni^{3+} ($t_{2g}^6e_g^1$), leading to a significant increase in e_g orbital occupancy.[106] As illustrated in Fig. 11d, the orbital hybridization between Ni and O_2 is analyzed. Compared to the antibonding orbitals $(d_{z^2}–\sigma)^*$ and $(d_{xz}/d_{yz}–2\pi)^*$ in NiII-NCF, the $(d_{z^2}–\sigma)^*$ orbital in NiIII-NCF exhibits a higher energy level with lower electron occupancy, which favors oxygen adsorption and enhances the Ni^{3+}–O_2 interaction. Bader charge analysis reveals that NiIII-NCF (Fig. 11f) transfers more electrons (0.26 e^-) to O_2 compared to NiII-NCF (0.21 e^-) (Fig. 11e), thereby enabling stronger O_2 activation and an increased electron transfer rate. The high affinity of Ni^{3+} sites toward the LiO_2 intermediate facilitates the formation of nanosheet-like Li_2O_2 within the voids between NiIII-NCF nanowires. As a result, Li–O_2 batteries based on the NiIII-NCF cathode exhibit a remarkably high specific capacity of 16 800 mA h g^{-1} and stable cycling performance exceeding 200 cycles. Similarly, in $ZnCo_2O_4$ spinel structures, high-temperature calcination induces a transition of cobalt ions from a low-spin state ($t_{2g}^6e_g^0$) to a high-spin state ($t_{2g}^4e_g^2$), significantly increasing the delocalization of e_g orbital electrons (Fig. 11g). This enhancement facilitates spin-selective charge transfer during the ORR/OER process and accelerates reaction kinetics through the formation of spin channels.[144]

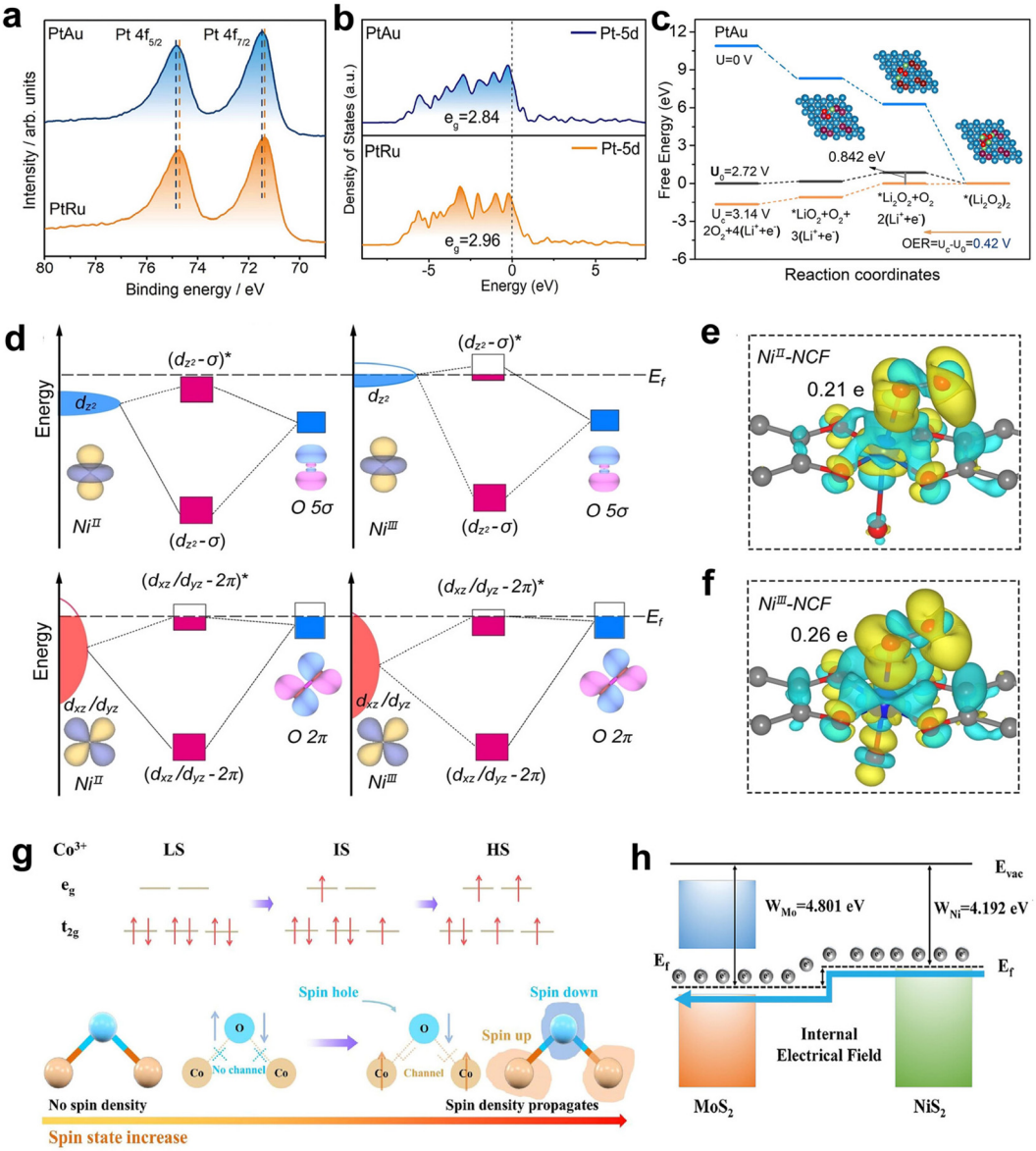

Fig. 11 (a) XPS spectra of the Pt 4f region for PtAu and PtRu cathodes. (b) PDOS of the Pt 5d orbitals in PtRu and PtAu. (c) Free energy profiles of the PtAu cathode under different potentials. The inset illustrates the optimized crystal structures of PtAu with specific adsorbates at the corresponding reaction steps.[107] (d) Schematic representation of the interaction between adsorbed O_2 and the d_{z^2} and $d_{xy/yz}$ orbitals of the Ni site in NiIII-NCF and NiII-NCF. Differential charge density distribution for O_2 adsorption on (e) NiII-NCF and (f) NiIII-NCF.[106] (g) Schematic diagram illustrating different spin states of Co^{3+} and the formation of the Co–O–Co spin channel with increasing Co^{3+} spin state.[144] (h) Work functions of MoS_2 and NiS_2, along with a schematic depiction of the formation of an internal electric field.[146]

Heterostructures regulate the electronic distribution of catalysts through interfacial effects, serving as another critical strategy for optimizing e_g orbital occupancy. In Ni/Mn-MOF, Mn doping further enhances the e_g orbital occupancy of Ni, significantly improving electronic coupling between Ni and redox intermediates.[145] As a result, this battery achieves an exceptionally high specific capacity of 28 464 mA h g^{-1} at 100 mA g^{-1} while maintaining long-term cycling stability over 524 cycles. A hierarchical NiS_2–MoS_2 heterostructure nanorod, synthesized *via* hydrothermal and chemical vapor deposition methods, features abundant defects and a mesoporous structure.[146] The work function difference between NiS_2 (4.192 eV) and MoS_2 (4.801 eV) induces charge transfer from NiS_2 to MoS_2, leading to the formation of an internal electric field (Fig. 11h). This internal field optimizes the e_g orbital occupancy of Mo atoms, as electrons are partially captured by highly electronegative Ni atoms, thereby reducing antibonding orbital occupancy. Consequently, the system achieves a balanced adsorption strength for oxygen intermediates (LiO_2, Li_2O_2). The Li–O_2 battery based on the NiS_2–MoS_2 cathode exhibits a coulombic efficiency of 99.65% and maintains stable performance even after 450 cycles at 1000 mA g^{-1}.

3.4 Orbital hybridization

In recent years, catalyst design based on orbital hybridization strategies has achieved breakthrough progress in the field of Li–O_2 batteries.[118,150,151] In the spinel-structured $MnCr_{0.5}Co_{1.5}O_4$, the introduction of Cr^{3+} at octahedral sites extends the Co^{3+}–O bond length and reduces lattice symmetry, leading to enhanced Co–O bond covalency.[96] This increased metal–oxygen covalency accelerates charge transfer in oxygen-related reactions, thereby promoting the reversible deposition and decomposition of Li–O_2 battery discharge product. Orbital hybridization can also be effectively tuned by modifying the coordination environment of metal centers.[112,134,152] In the single crystalline naphthalene lead MOF (Na–Pb-MOF), which features seven-coordinated PbO_7 nodes, the Pb–O bond length (2.88 Å) is longer than that in the six-coordinated PbO_6 nodes of the tetramethoxy lead MOF (4OMe-Pb-MOF) (2.37 Å).[112] This elongation weakens the coupling between Pb 5d and O 2p orbitals, optimizing orbital interactions and improving the adsorption properties of intermediates such as LiO_2 (Fig. 12a and b). Consequently, this enhancement lowers the activation energy for both LiO_2 reduction to Li_2O_2 and LiO_2 oxidation to O_2 (Fig. 12c), significantly reducing the overall battery overpotential (0.52 V) and enabling stable cycling performance over 140 cycles.

Rare-earth elements play a unique role in band hybridization due to their inner-shell orbitals and the strong localization of 4f electrons.[101,108,153,154] In the Ce single-atom-anchored CoO system (Ce_1/CoO), Ce 4f and Co 3d orbitals undergo hybridization mediated by oxygen bridges, forming a dynamic electron reservoir that flexibly regulates the adsorption–desorption equilibrium of reaction intermediates.[108] As illustrated in Fig. 12d, *in situ* SERS reveals reversible changes

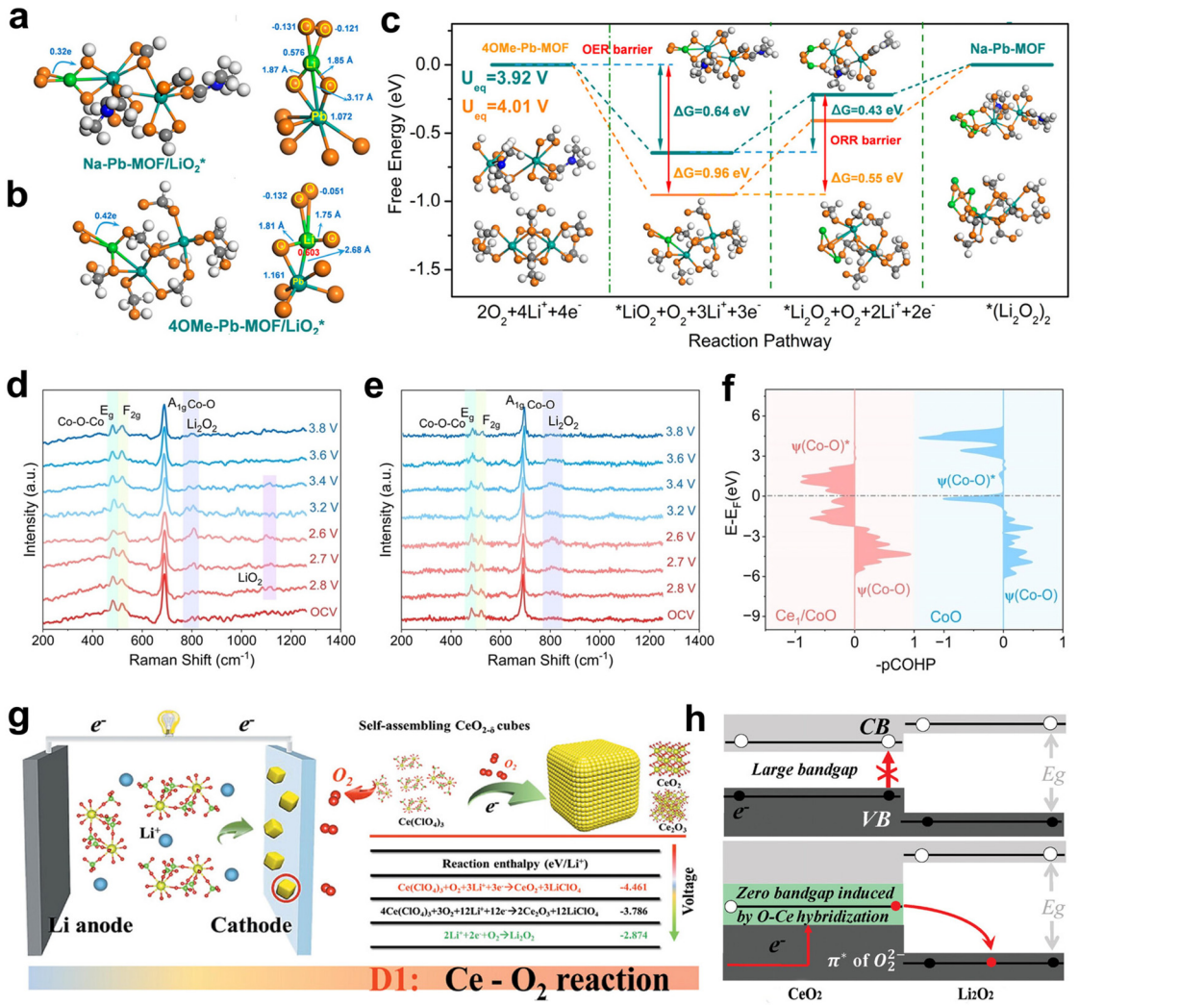

Fig. 12 (a) Bader charge analysis of LiO_2 adsorption on Na–Pb-MOF and (b) 4OMe-Pb-MOF. (c) Gibbs free energy curves of Na–Pb-MOF and 4OMe-Pb-MOF. The inset illustrates the optimized crystal structures of adsorbates at different reaction steps.[112] (d) Surface-enhanced *in situ* SERS of Ce_1/CoO and (e) CoO cathodes. (f) Crystal orbital Hamilton population (COHP) analysis of the Co–O bond in Ce_1/CoO and CoO.[108] (g) DFT calculations and schematic representation of CeO_2/Ce_2O_3/Li_2O_2 formation during discharge. (h) Schematic representation of charge transfer from CeO_2 to the O_2^{2-}-π* energy level in Li_2O_2.[101]

in the Raman signals of the Ce_1/CoO cathode during charge–discharge cycles. The characteristic O–Co–O bending (E_g) and Co–O stretching (A_{1g}) vibrations gradually weaken, suggesting increased surface disorder and distortion of the CoO_6 octahedral structure, thereby maintaining a highly active state. This indicates that Ce_1/CoO facilitates self-regulating catalysis throughout the Li–O_2 battery cycling process. In contrast, after a single charge–discharge cycle, the E_g/A_{1g} Raman peak intensities of CoO fail to return to their initial state, suggesting potential surface reconstruction or loss of active sites (Fig. 12e). As shown in Fig. 12f, compared to CoO (ICOHP = −0.66 eV), the Ce_1/CoO system exhibits a richer bonding state between Co and coordinated oxygen atoms (ICOHP = −0.70 eV). This indicates an increased number of Co–O bonding orbitals and their enhanced occupancy below the E_F, ensuring the stability of Co–O bonds under redox conditions. Benefiting from the enhanced orbital coupling, the Ce_1/CoO cathode delivers an ultra-high discharge capacity of 37 462 mA h g^{-1} at a current density of 250 mA g^{-1}, representing a 125% and 750% increase compared to CoO (16 629 mA h g^{-1}) and CeO_2 (4408 mA h g^{-1}) cathodes, respectively (Fig. 12g). An *in situ* electrochemical strategy was employed to synthesize a metastable $CeO_{2-\delta}$ catalyst, where the cerium–oxygen reaction ($Ce^{3+} + O_2 + e^- \rightarrow CeO_{2-\delta}$) occurs between Ce^{3+} in the electrolyte and O_2, forming oxygen vacancy-rich $CeO_{2-\delta}$ nanocubes with high-energy (311) crystal facets (Fig. 12g).[101] By optimizing the O–Ce hybridized electronic structure, an electronic transport bridge was established between lattice oxygen and neighboring cerium atoms, creating a direct charge transfer channel from the Ce-4f orbitals in CeO_2 to the O_2^{2-}–π* orbitals in Li_2O_2 (Fig. 12h). This facilitated Li–O_2 reactions, leading to the formation of submicron Li_2O_2 shell layers, thereby unlocking the capacity limitations of Li–O_2 batteries. As a result, the discharge capacity increased significantly to 32 015 mA h g^{-1} at 250 mA g^{-1}, far surpassing that of conventional CeO_2 based cathodes (5703 mA h g^{-1}).

The study of intermetallic compounds[115] and single-atom alloy[40,155] catalysts has introduced innovative pathways in orbital hybridization strategies. Pd_3Pb nanocubes synthesized *via* a wet-chemistry method exhibit an ordered intermetallic structure, where Pd single atoms are uniformly dispersed within a Pb matrix, forming stable Pd–Pb covalent bonds.[112] Intra-molecular hybridization between the Pd 4d orbitals and Pb 6p orbitals lowers the d-band energy level of Pd (Fig. 13a), leading to an increase in the oxidation state of Pd. As shown in Fig. 13b and c, the influence of intra-molecular d–p hybridization results in a reduced overlap between the bonding and anti-bonding states of the Pd $4d_{z^2}$–5σ and $4d_{xy}/d_{yz}$–2π* orbitals upon LiO_2 adsorption. This weakens the orbital interaction with LiO_2. By leveraging both intra-molecular p–d orbital hybridization (direct coupling between Pd 4d and Pb 6p orbitals within Pd_3Pb) and inter-molecular orbital hybridization (interaction between Pd 4d and LiO_2 5σ/2π* orbitals), a cascade electron regulation system is established, effectively optimizing the electronic structure of the catalyst (Fig. 13d). This cascade-oriented orbital hybridization in Pd_3Pb enables an ultra-low OER overpotential of 0.45 V in Li–O_2 batteries, achieving outstanding cycling stability over 175 cycles at a fixed capacity of 1000 mA h g^{-1}. A Pt_1Pd single-atom alloy catalyst was synthesized *via* a one-step wet-chemistry method. As shown in Fig. 13e, Pt atoms are uniformly dispersed within ultrathin Pd hexagonal nanosheets, occupying Pd lattice sites in a single-atom form and forming stable Pt–Pd covalent bonds.[40] The ELF (Fig. 13f) and Bader charge analysis (Fig. 13g) reveal that Pt single-atom sites exhibit electron enrichment (−0.23*e*), while Pd sites experience electron depletion (+0.03*e*), resulting in a strong electronic localization effect. This electronic redistribution facilitates the activation of the O_2/Li_2O_2 redox couple, effectively lowering the energy barriers for the ORR and OER. As illustrated in Fig. 13h, O_2 preferentially adsorbs at Pt sites, promoting the two-step reduction process of $LiO_2 \rightarrow Li_2O_2$ while suppressing the formation of byproducts such as Li_2CO_3. These findings provide an important theoretical framework for the design of highly efficient Li–O_2 battery cathode catalysts based on orbital engineering. By precisely tuning metal oxygen bonding characteristics,[101,108,151,156] local electronic structures at active sites,[96,150,157] and orbital coupling strength,[40,112] this strategy offers a pathway to overcoming limitations in reaction pathway control and stability that challenge conventional catalysts.

3.5 Crystal face engineering design

Regulating the deposition pathway of discharge products through rational catalyst design has been widely employed to control the morphology and structure of Li_2O_2. Given that the ORR/OER reactions occur at the surface of oxygen catalysts, cathode catalyst facet engineering is considered an effective approach to enhance catalytic activity and modulate the deposition/decomposition pathway of discharge products by exposing specific crystal facets.[99,158–160] Studies have shown that two-dimensional Mn_3O_4 nanosheets supported on graphene preferentially expose the (101) facet. The adsorption energy of Li_2O_2 on the Mn_3O_4 (101) facet (−2.16 eV) is significantly lower than that on the (211) facet (−5.67 eV), indicating that the (101) facet facilitates the desorption of Li_2O_2 and reduces the decomposition energy barrier.[119] By exposing the (101) facet and introducing oxygen vacancies, Mn_3O_4 NS/G effectively reduces the adsorption energy of Li_2O_2, lowers the charge overpotential to 0.86 V, and achieves an ultrahigh specific capacity of 35 583 mA h g^{-1} at 200 mA g^{-1}. Similarly, two-dimensional layered structures with chemical bonding, such as stacked Ag–Te tetrahedral layers, predominantly expose the Ag-terminated (200) crystal facet.[161] The (200) facet exhibits adsorption energies of 0.487 eV and 0.963 eV for LiO_2 and Li_2O_2, respectively, indicating physical adsorption. This facilitates the efficient formation of Li_2O_2 *via* a two-electron pathway, as supported by the Δ*G*–*U* phase diagram, which reveals a voltage window of 2.27–2.31 V (Fig. 14a–c). In contrast, the (102) facet exhibits stronger adsorption (weaker chemical adsorption), which suppresses Li_2O_2 conversion. The narrow-bandgap telluride Ag_2Te successfully mitigates the facet-dependent catalytic anisotropy, with both the 2D stacked surface (200) plane and the side-

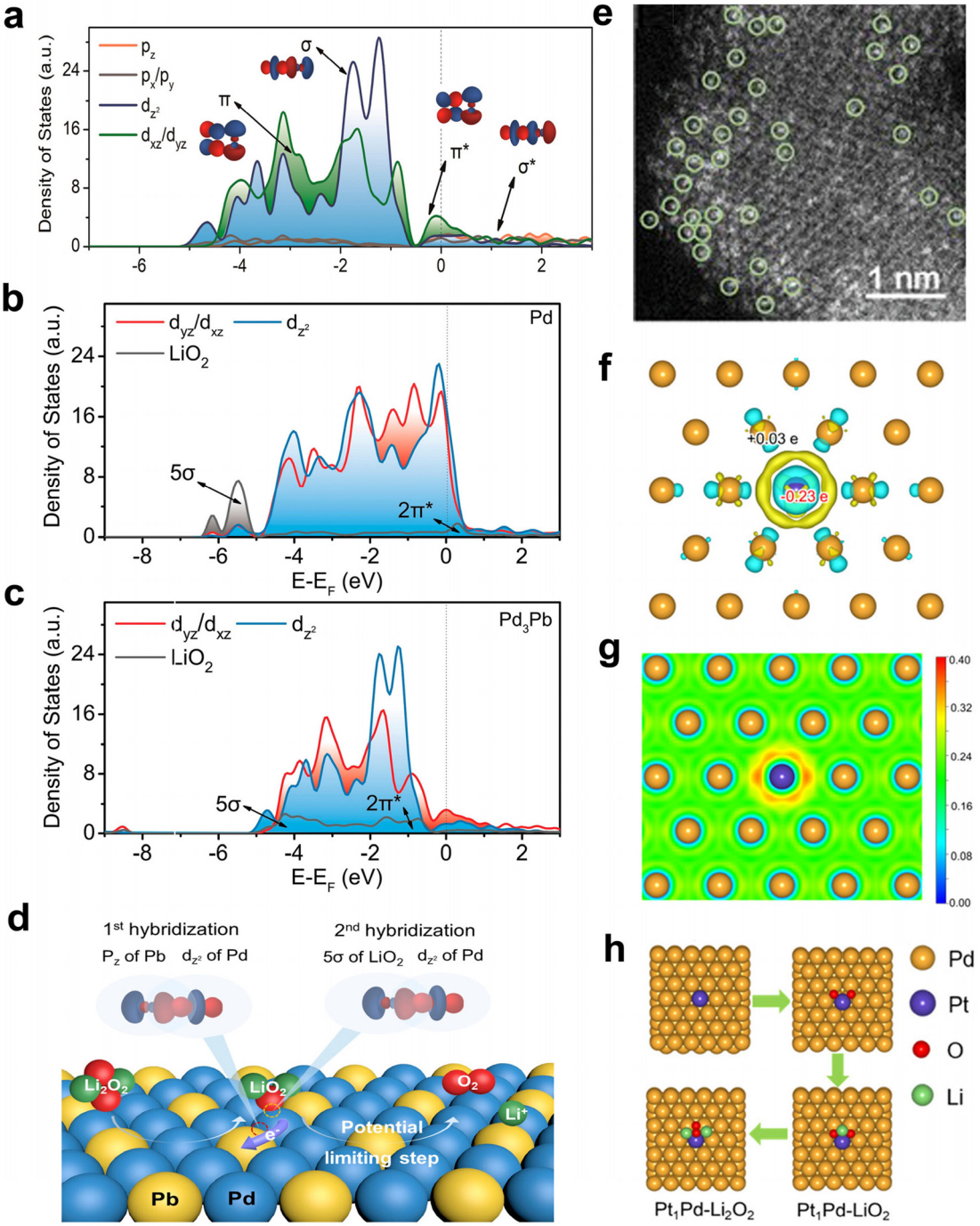

Fig. 13 (a) DOS of Pd d_{z^2}, $d_{xz/yz}$ orbitals and Pb p_x, p_y, p_z orbitals after intra-molecular p–d orbital hybridization in Pd_3Pb. (b) DOS of Pd 4d $d_{yz}/d_{z^2}/d_{xz}$ orbitals in Pd. (c) DOS of Pd 4d $d_{yz}/d_{z^2}/d_{xz}$ orbitals in Pd_3Pb with adsorbed LiO_2. (d) Schematic representation of cascade orbital-oriented hybridization from intra-molecular Pb–Pd p–d hybridization in Pd_3Pb to inter-molecular orbital hybridization between Pd_3Pb (Pd $4d_{xz/yz}$ and $4d_{z^2}$) and LiO_2 (2π* and 5σ), using the d_{z^2} orbital along the *z*-axis as an example.[115] (e) AC-HAADF-STEM image of the Pt_1Pd alloy (single-atom Pt marked with green circles). (f) ELF values of Pt_1Pd. (g) Charge density difference distribution (regions of electron enrichment and depletion) in Pt_1Pd. (h) Schematic representation of the discharge pathway of a Li–O_2 battery on the Pt_1Pd surface.[40]

plane exhibiting exceptional catalytic activity. As a result, Li–O_2 batteries based on the Ag_2Te cathode demonstrate an ultra-long cycling lifespan of over 300 cycles at a high current density of 500 mA g^{-1}, with a fixed capacity of 1000 mA h g^{-1}.

Crystal facet engineering, as an important strategy to regulate the deposition pathways of discharge products and enhance catalytic performance in Li–O_2 batteries, demonstrates significant application potential.[162–164] By precisely

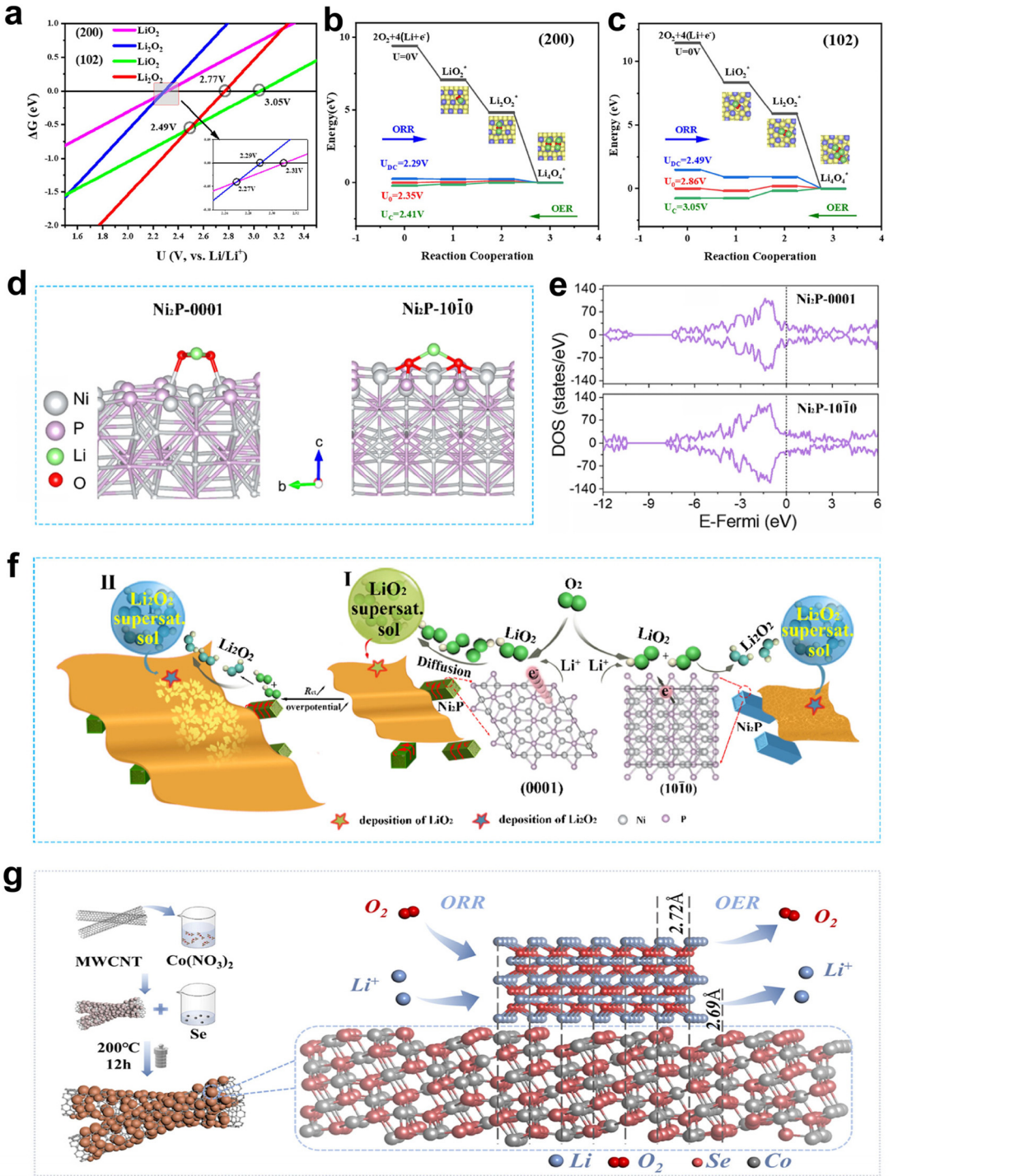

Fig. 14 (a) Reaction phase diagram of the Ag_2Te cathode on the (200) and (102) crystal facets. (b) Gibbs free energy diagram of the Ag_2Te(200) and (c) (102) crystal facet during the ORR/OER process.[161] (d) Comparison of adsorption energies of the LiO_2 intermediate on Ni_2P(0001) and (1010) crystal facets. (e) DOS analysis of Ni_2P(0001) and (1010) crystal facets. (f) Schematic representation of the nucleation and growth mechanisms of discharge products on Ni_2P(0001) and (1010) crystal facets.[160] (g) Synthesis pathway of $Co_{0.85}Se$@CNT and schematic illustration of the lattice matching between the $Co_{0.85}Se$(101) crystal facet and the Li_2O_2(100) crystal facet.[165]

controlling the exposed orientation of catalyst facets and their surface electronic structures, it is possible not only to modulate the adsorption behavior of intermediates such as LiO_2 and Li_2O_2 but also to induce the formation of discharge products with specific morphologies, thereby alleviating electrode passivation. Moreover, integrating oxygen vacancy introduction, lattice matching effects, and porous structure design can further optimize the distribution of active sites, reduce polariz-

ation, and improve cycling stability. This approach provides both theoretical insights and practical pathways for the development of highly efficient and stable cathode materials for Li–O_2 batteries.

Crystal-facet-controlled Ni_2P nanorods were synthesized on Ni foam *via* a hydrothermal-phosphorization strategy, effectively regulating the nucleation, growth, and morphology of LiO_2 and Li_2O_2.[160] DFT calculations reveal that the adsorption energies of LiO_2 on the Ni_2P(0001) and (1010) facets are −0.42 eV and −1.87 eV, respectively (Fig. 14d). Compared to the (1010) facet, the (0001) facet exhibits a higher DOS near the Fermi level, indicating a stronger electron transport capability for the Ni_2P-0001 cathode (Fig. 14e). As illustrated in Fig. 14f, Ni_2P-0001, which preferentially exposes the (0001) facet, induces the formation of large-sized Li_2O_2 sheet-like and porous nanostructures due to its weak LiO_2 adsorption energy and high electron transport rate. This mitigates the passivation effect caused by insulating discharge products. Therefore, the deposition behavior and morphology of discharge products can be effectively tuned by controlling the preferentially exposed facets of the Ni_2P catalyst.

The lattice matching effect is also an important strategy for regulating facet exposure properties. As illustrated in Fig. 14g, the grain-refined $Co_{0.85}Se$@CNT catalyst exhibits a (101) facet with a lattice spacing of 2.69 Å, which is highly matched with the (100) facet of Li_2O_2 (2.72 Å).[165] This strong lattice matching serves as a template for the epitaxial growth of Li_2O_2, promoting its oriented formation while suppressing the generation of side products. As a result, Li–O_2 batteries based on the $Co_{0.85}Se$@CNT cathode demonstrate exceptional cycling stability of over 2400 hours at a current density of 100 mA g^{-1}.

4. Innovative strategies in enhancing catalytic performance

External field-assisted strategies offer innovative approaches to overcoming the intrinsic activity limitations of cathode catalysts in Li–O_2 batteries. By introducing energy inputs such as light,[166–168] electricity,[169] magnetism,[41,120] or heat,[75] it is possible to dynamically regulate the local electronic structure at the catalyst interface, carrier distribution, and reaction kinetics. These modulations significantly enhance the activity and stability of both the ORR and OER. Unlike conventional chemical modifications, external fields enable real-time and directional control of the catalytic process through non-contact intervention. This approach has shown particular advantages in addressing key challenges such as high overpotentials and poor cycling stability. In recent years, the emergence of novel strategies, including photo-electrochemical synergistic catalysis, magnetothermal-induced lattice vibrations, and piezoelectric field-enhanced charge separation, has not only deepened the understanding of multiphysics coupling mechanisms but also accelerated the transition of Li–O_2 batteries from passive energy storage systems to intelligent, responsive platforms.

Photo-assisted strategies have emerged as an innovative approach to addressing Li–O_2 battery challenges, as they can enhance the kinetics of redox reactions through the synergistic effect of photo-generated electron–hole pairs.[170–174] A study on facet-controlled WO_3 photoanodes revealed that by increasing the proportion of exposed (002)/(020) crystal facets in the WO_3 photoelectrode, a controllable transition from the solution-growth mode to the surface-growth mode of Li_2O_2 formation can be achieved (Fig. 15a).[175] Furthermore, the Li_2O_2 layer deposited during the discharge process can form a Z-type heterojunction with WO_3. This photo-assisted discharge process occurs in three stages, as shown in Fig. 15b: (I) initial stage: the photo-generated electrons from WO_3 are consumed to reduce O_2, forming a thin Li_2O_2 film on the electrode surface; (II) thickening stage: the Li_2O_2 layer formed interacts with WO_3 to create a Z-type heterojunction, which promotes exciton dissociation and generates free electrons, further accumulating discharge products; (III) termination stage: as Li_2O_2 continues to accumulate, its enhanced exciton binding energy inhibits carrier separation, ultimately leading to the termination of the discharge process. Ultimately, the WO_3 photoanode, dominated by the (002) facet, achieves an extremely low overpotential of 0.07 V and maintains high cycling stability for over 200 hours.

Interface engineering and heterojunction construction have further enriched the electronic modulation strategies for photocatalysts. A composite cathode containing oxygen vacancies, Ag/Bi_2MoO_6 (denoted as AB-OV/CC), demonstrates enhanced full-spectrum light absorption from ultraviolet to visible regions through the synergistic effects of Ag's localized surface plasmon resonance (LSPR) and the oxygen vacancies in Bi_2MoO_6.[176] The LSPR-generated hot electrons from Ag are injected into the oxygen vacancies band of Bi_2MoO_6, rather than its conduction band, enabling efficient charge separation (Fig. 15c). The accelerated oxygen reaction kinetics lead to the formation of amorphous Li_2O_2, resulting in an elevated discharge plateau voltage of 3.05 V. During charging, photoexcited holes rapidly decompose the amorphous Li_2O_2, lowering the charge plateau voltage to 3.25 V. This enables a high initial round-trip efficiency of 93.8% (Fig. 15d). An S-type heterojunction photoelectrode based on Fe_2O_3/C_3N_4 was constructed, in which interfacial Fe–N bonds (bond length: 2.42 Å) and an internal electric field (IEF) synergistically promote directional separation of photo-generated charge carriers.[177] This structure establishes a unique electron transport pathway with spatially separated redox centers, where photoelectrons are concentrated on C_3N_4 and photogenerated holes on Fe_2O_3. During discharge, electrons in the conduction band of C_3N_4 reduce O_2 to form LiO_2 intermediates, which further convert into Li_2O_2, while holes in the valence band of Fe_2O_3 participate in the oxidation reaction. During charging, holes in Fe_2O_3 oxidize Li_2O_2 to O_2, while electrons in C_3N_4 reduce Li^+ to metallic lithium (Fig. 15e). This design achieves a high discharge voltage of 3.13 V and a low charge voltage of 3.19 V, resulting in a round-trip efficiency approaching 98%.

Photocatalytic technologies also offer new perspectives for dynamically regulating discharge products in Li–O_2 batteries.

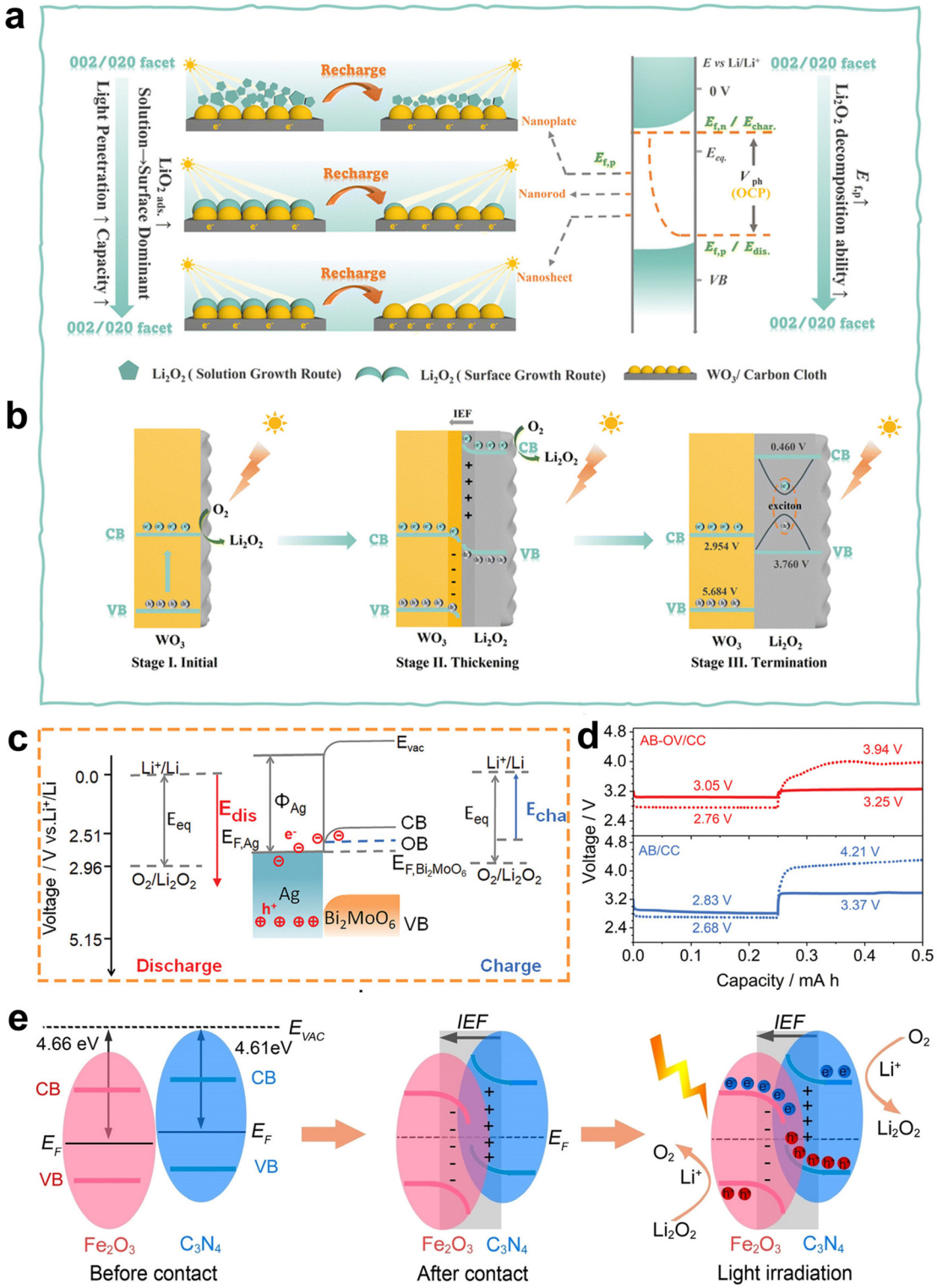

Fig. 15 (a) Facet-controlled Li_2O_2 growth pathways and the photocatalytic activity of WO_3 in photo-assisted Li–O_2 batteries. (b) Proposed mechanism of the photo-assisted discharge process, consisting of three distinct stages.[175] (c) Reaction mechanism of the AB-OV/CC photo-cathode in photo-assisted Li–O_2 batteries. (d) Discharge/charge profiles of AB-OV/CC and AB/CC photo-cathodes at a current density of 50 mA g^{-1} under illuminated (solid lines) and dark (dashed lines) conditions.[176] (e) Schematic illustration of directional charge transfer induced by the internal electric field at the Fe_2O_3/C_3N_4 interface.[177]

By employing a cathode composed of light-responsive gold nanoparticles exhibiting SPR, combined with reduced graphene oxide (Au/rGO), recent studies have revealed the critical role of matching ORR kinetics with lithium-ion transport rates in determining battery performance.[178] Under light irradiation, this system significantly alleviates the phenomenon of "sudden battery death" caused by Li^+ concentration polarization, introducing a novel concept of dynamic control. Furthermore, a porphyrin-based MOF incorporating $(Fe_2Ni)O(COO)_6$ clusters has been used as a photo-cathode to substantially enhance the performance of photo-assisted Li–O_2 batteries.[179] The coupling between Ni 3d and Fe 3d orbitals strengthens ligand-to-metal cluster charge transfer (LMCT), thereby promoting the separation of excitons into free charge carriers. This process effectively suppresses recombination of photo-generated electron–hole pairs and activates the gene-

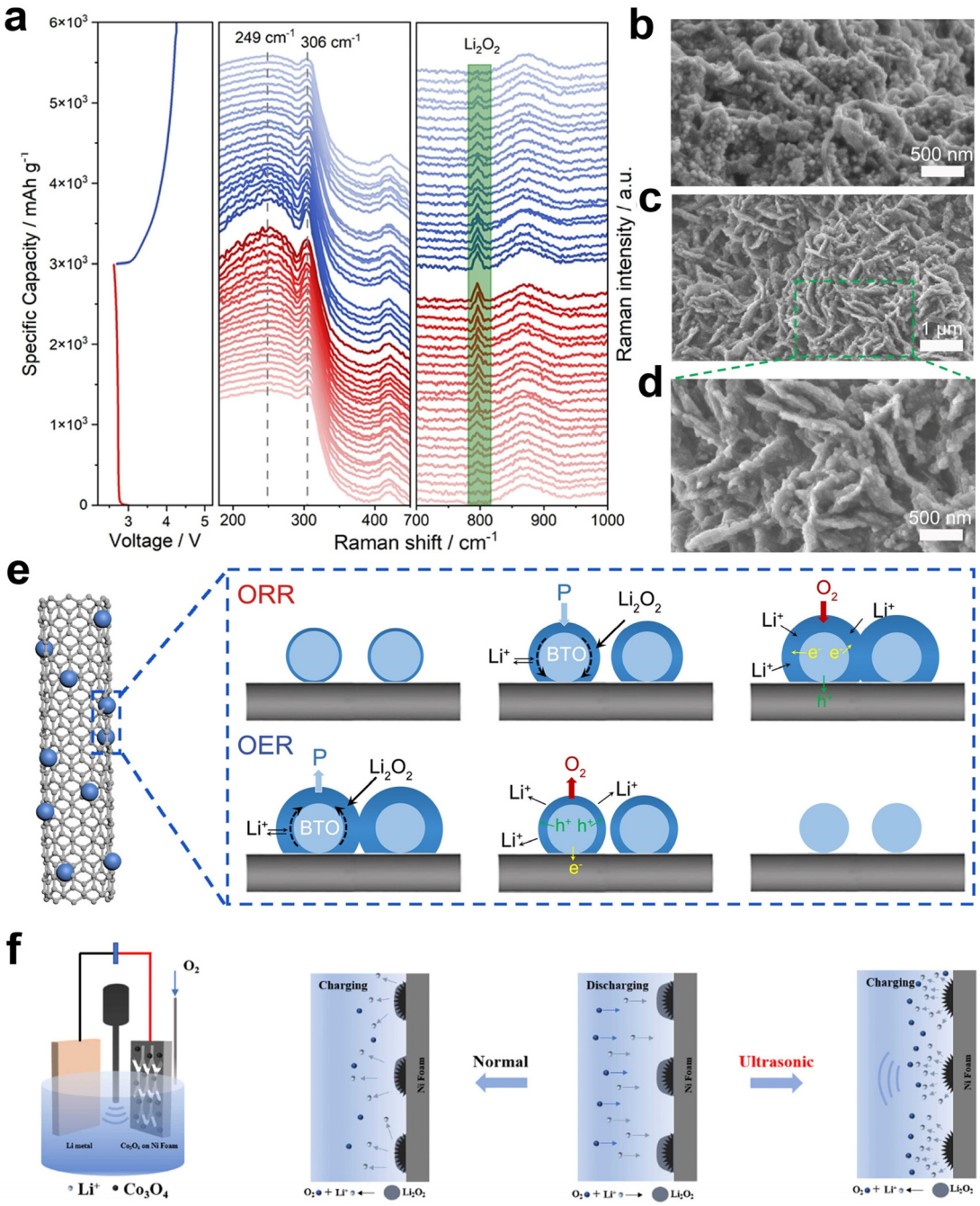

Fig. 16 (a) *In situ* electrochemical Raman spectra collected on the BTO-CNT cathode at a current density of 300 mA g^{-1}. (b) SEM image of the BTO-CNT cathode at a discharge depth of 1500 mA h g^{-1} and a current density of 300 mA g^{-1}. (c and d) Low- and high-magnification SEM images of the BTO-CNT cathode at a discharge depth of 3000 mA h g^{-1} under a current density of 300 mA g^{-1}. (e) Schematic illustration of Li_2O_2 formation and decomposition on the BTO surface.[169] (f) Schematic diagram of the ultrasonic charging mechanism on the electrode surface.[180]

ration of O_2^-, rather than $^1O_2$. Under light irradiation of 100 mW cm^{-2}, the FeNi-TCPP-based photo-assisted Li–O_2 battery achieves a remarkably low overall overpotential of 0.28 V and a round-trip efficiency of 92%.

In addition to photo-assisted catalysis,[174,181–183] researchers have explored a broader range of external field-assisted strategies.[120,180] One such innovative approach utilizes a stress field, with $BaTiO_3$ (BTO) piezoelectric material as the core.[169] As shown in Fig. 16a, Raman scattering peaks at 249 cm^{-1} and 306 cm^{-1} correspond to the symmetric and asymmetric crystal structures of BTO. During discharge, Li_2O_2 products rapidly accumulate on the surface of BTO (Fig. 16b–d), and the Raman scattering peaks at 249 cm^{-1} and 306 cm^{-1} are significantly enhanced, indicating increased lattice distortion of BTO. This is attributed to the intrinsic stress generated by the continuous accumulation of Li_2O_2, which causes Ti^{4+} ions to shift along specific crystal axes toward the O^{2-} direction. Consequently, the O^{2-} ions undergo electronic polarization displacement, generating a spontaneous polarization electric field that drives carrier separation and transport. This allows for the continuous separation and accumulation of electrons and holes, while the conduction and valence bands are tilted to favor enhanced ORR and OER kinetics (Fig. 16e). This coupling strategy between intrinsic stress and electric field at the surface effectively accelerates the interfacial transport rate of Li^+ and improves the redox reaction kinetics in Li–O_2 batteries. The study on Co_3O_4 grown on nickel foam as a cathode explores the impact of acoustic fields on the performance of Li–O_2 batteries.[180] Ultrasonic charging plays a positive role in enhancing mass transfer processes, suppressing concentration polarization, promoting the rapid decomposition of Li_2O_2, and increasing the exposure of active sites (Fig. 16f). Ultrasonic energy, which can be converted into mechanical and thermal energy, aids in the decomposition of Li_2O_2, exposing more active sites and enhancing the rate of the OER. Experimental results demonstrate that under ultrasonic charging conditions with a duty cycle of 5 : 5 and a power of 675 W, the overpotential is reduced by 25.9%, and the battery's cycle life is extended from the typical 67 cycles to 321 cycles.

Magnetic field-assisted strategies have shown promising potential among multi-field coupling technologies due to the unique Lorentz force effect, which can suppress the rapid recombination of photoexcited electrons and holes. A three-dimensional porous NiO nanosheet on nickel foam (NiO/FNi) was employed as a photoelectrode.[120] As a p-type semiconductor, NiO/FNi generates photoinduced electrons and holes under illumination. As illustrated in Fig. 17a, electrons in the conduction band (CB, 2.04 V *vs.* Li^+/Li) facilitate the ORR, while holes in the valence band (VB, 5.16 V *vs.* Li^+/Li) accelerate the oxidation of Li_2O_2 during the OER, thereby reducing both discharge and charge overpotentials. When an external magnetic field (5 mT) is applied, the Lorentz force acts in opposite directions on the photoexcited electrons and holes, effectively suppressing their recombination (Fig. 17b). Serving as an integrated bifunctional photo-cathode, NiO/FNi combines magnetic effects with photoelectric conversion capabilities, enabling effective regulation of internal electrochemical properties, charge and lithium-ion transport, and redox reac-

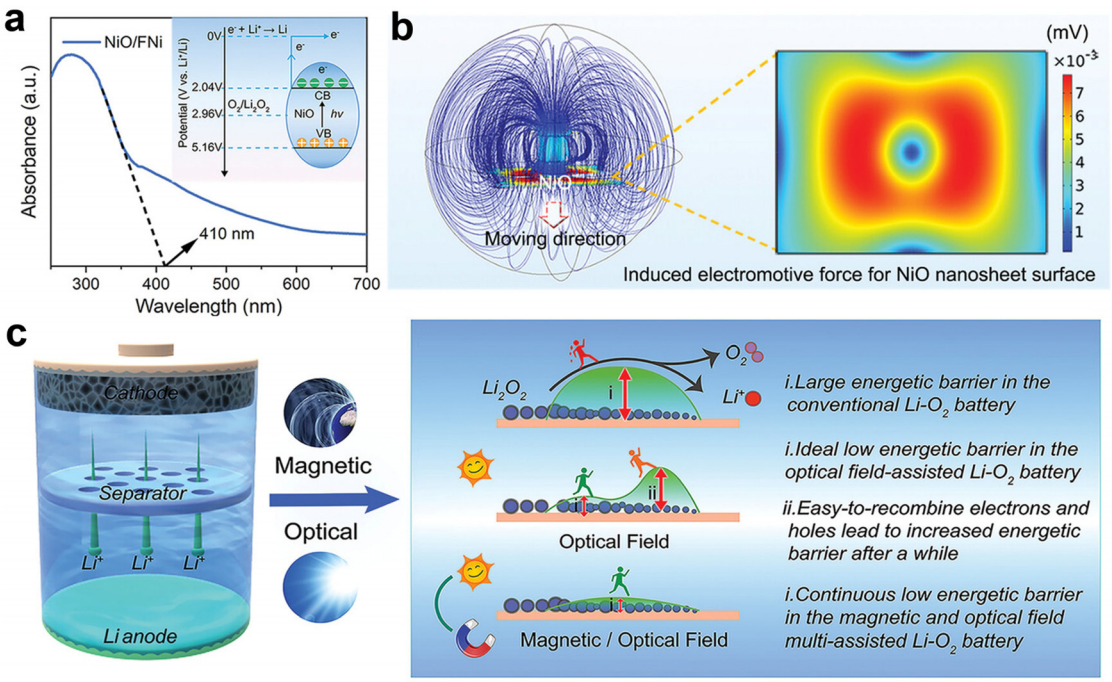

Fig. 17 (a) UV-vis absorption spectrum of NiO/FNi. Inset: energy band diagram of NiO/FNi. (b) Schematic illustration of the induced electromotive force (EMF) in NiO under relative motion within a magnetic field, along with a COMSOL simulation of the surface EMF distribution on NiO under magnetic assistance. (c) Schematic diagram of the working mechanism of a Li–O_2 battery under combined light and magnetic field assistance.[120]

tion kinetics within the battery (Fig. 17c). The device operates stably at an ultra-low charging voltage of 2.73 V and achieves a high energy efficiency of 96.7% along with excellent cycling stability.

Field-assisted strategies, by dynamically modulating reaction kinetics and interfacial behaviors in batteries, hold theoretical promise for overcoming the intrinsic performance limitations of conventional catalysts.[184,185] However, their practical implementation still faces multiple challenges, including device integration, energy efficiency, cost control, and engineering scalability. At present, the coupling of external fields with electrochemical systems is not yet suitable for large-scale fabrication or industrial deployment. For instance, magnetic field-assisted strategies often require embedding permanent magnets or electromagnetic coils within the battery, which not only increases the device's volume and weight but may also induce variations in reaction site selectivity due to magnetic field gradients within porous electrodes. This necessitates complex magnetic shielding or gradient field designs for effective control. In the case of light-field strategies, the introduction of transparent windows (*e.g.*, quartz or flexible polymers) into the battery casing can compromise system sealing, increasing the risk of electrolyte leakage and ambient gas permeation. Moreover, the uneven distribution and attenuation of light within porous structures can result in non-uniform activation of catalytic sites, limiting the overall reaction efficiency. Traditional photocatalysts are also prone to activity loss under prolonged illumination due to lattice oxygen depletion induced by photogenerated holes. More critically, the application of external fields typically requires additional energy inputs, such as light sources or electromagnetic devices, leading to relatively high power consumption and poor overall energy conversion efficiency.[186,187] Therefore, key directions for future research include the design of highly responsive materials, the development of energy recovery mechanisms, and the use of green energy sources to power the external fields, all aimed at improving system efficiency and promoting practical viability.

5. Conclusion and future perspectives

In recent years, significant progress has been made in the design and performance optimization of cathode catalysts for Li–O_2 batteries, laying a critical foundation for enhancing energy efficiency, cycling stability, and practical application potential. This review begins with an overview of the basic reaction mechanisms in Li–O_2 batteries, systematically summarizing the key role of cathode catalyst electronic properties in modulating the ORR and OER kinetics, as well as the corresponding structure–activity relationships based on current core research findings and innovative strategies. Through breakthroughs in DFT calculations and *in situ* characterization techniques, research has revealed the intrinsic relationships between catalyst electronic structures, such as the metal d-band center, non-metallic p-orbital sites, e_g orbital occupancy, orbital hybridization, optimization of exposed facets, and external field-assisted strategies. These insights progressively highlight the close connection between catalyst electronic structure and reaction activity, providing important theoretical support for the advancement of Li–O_2 battery technology and the rational design of efficient cathode catalysts. Notably, innovative strategies, including external field-assisted technologies such as light, sound, electricity, and magnetism, offer new dimensions for improving catalytic efficiency, achieving performance breakthroughs beyond traditional thermodynamic limitations.

Despite the remarkable progress in the design of cathode catalysts for Li–O_2 batteries, several critical areas still require further investigation to advance the practical application of this technology.

Future research should focus on the precise modulation of catalyst electronic structures at the molecular and atomic levels, with the goal of establishing quantitative structure–activity models that correlate adsorption free energy, electron transfer numbers, and catalytic activity. Such models will provide a fundamental basis for enhancing the kinetics of the ORR and OER and guide the rational design of high-performance cathode catalysts. Electronic structure optimization should not be limited to the modification of individual materials; instead, future efforts can explore the integration of different catalytic components. Designing composite materials or heterointerfaces to leverage synergistic effects between components can further improve catalytic performance. For example, metal–carbon composite materials can significantly enhance electrical conductivity and reaction kinetics. Moreover, emerging strategies such as external field-assisted catalysis and solid-state battery systems have shown great potential for improving both catalytic efficiency and long-term stability.

Although correlations between the electronic states of cathode catalysts and their catalytic activity can be established, such structure–activity relationships do not fully capture the actual reaction mechanisms. Under operating conditions, the nanoscale structures and coordination environments of active sites often undergo dynamic changes, diminishing the relevance of performance relationships derived solely from the catalyst's initial state. Therefore, the integration of advanced *in situ* characterization techniques is essential. For example, *in situ* X-ray absorption fine structure (XAFS) spectroscopy can identify the true active sites on electrode surfaces; *in situ* SERS enables the investigation of interfacial reactions and the capture of reaction intermediates during charge–discharge cycles; *in situ* UV-vis absorption spectroscopy allows monitoring of $^1O_2$ dynamics and associated parasitic reactions. Additionally, TOF-SIMS provides precise compositional and three-dimensional spatial analysis of discharge products. Moreover, the development of theoretical modeling methods under realistic working conditions, such as molecular dynamics simulations, enables real-time tracking of the evolution of catalyst surfaces, active sites, and intermediates

during reactions. These approaches help unravel reaction mechanisms and the dynamic nature of active sites. By integrating theoretical simulations with experimental studies, a deeper understanding of the formation and decomposition kinetics of Li_2O_2 can be achieved, offering a solid theoretical foundation for the design of next generation high efficiency catalysts.

The optimization of cathode, electrolyte, and anode interfaces must be pursued in a coordinated manner, encompassing the development of stable solid–liquid interfaces, enhancement of ionic conductivity, and improvement of interfacial durability and resistance to contamination. For example, electrolytes with low donor numbers tend to form thin Li_2O_2 films, making them suitable for applications requiring high stability, whereas high donor number electrolytes promote the formation of Li_2O_2 toroids, which are beneficial for achieving high discharge capacities. Therefore, it is essential to develop electrolytes that simultaneously offer high solubility and high diffusion coefficients. Catalyst degradation induced by reactive oxygen species, such as O_2^- and $^1O_2$, along with the accumulation of side products (Li_2CO_3 and LiOH), can significantly reduce charging efficiency and increase energy loss. Designing catalysts capable of converting $^1O_2$ into its less reactive triplet state ($^3O_2$) is key to suppressing these undesirable side reactions. The lithium metal anode, due to its high reactivity, readily reacts with electrolytes and oxygen, leading to dendrite formation and increased risk of short circuits. Strategies such as constructing artificial solid electrolyte interphase (ASEI) layers, introducing lithium host materials, and optimizing lithium stripping/plating mechanisms have proven effective in improving the cycling stability and safety of the anode.

Data availability

The data that support the findings of this study are available from the corresponding author upon reasonable request. All relevant data generated or analyzed during this study have been properly cited and referenced within the manuscript. Any additional data or materials can be made accessible to interested researchers, in accordance with the data sharing policies of EES Batteries.

Conflicts of interest

There are no conflicts to declare.

Acknowledgements

This work was supported by the Science and Technology Development Fund (FDCT) of Macao S.A.R (0033/2023/ITP1, 0022/2023/RIB1, 046/2019/AFJ and 0070/2023/AFJ), the Multi-Year Research Grants (file no. MYRG2022-00223-IAPME and MYRG-GRG2024-00166-IAPME) from the Research Services and Knowledge Transfer Office at the University of Macau.

References

1 J. Lu, Y. Lei, K. C. Lau, X. Luo, P. Du, J. Wen, R. S. Assary, U. Das, D. J. Miller, J. W. Elam, H. M. Albishri, D. A. El-Hady, Y. K. Sun, L. A. Curtiss and K. Amine, *Nat. Commun.*, 2013, **4**, 2383.
2 M. Saubanère, E. McCalla, J. M. Tarascon and M. L. Doublet, *Energy Environ. Sci.*, 2016, **9**, 984–991.
3 Y. Wang, N. Jiang, D. Pan, H. Jiang, Y. Hu and C. Li, *Chem. Eng. J.*, 2022, **437**, 135422.
4 S. Song, F. Yin, Y. Fu, J. Ren, J. Ma, Y. Liu, R. Ma and W. Ye, *Chem. Eng. J.*, 2023, **451**, 138818.
5 J. Lu, L. Cheng, K. C. Lau, E. Tyo, X. Luo, J. Wen, D. Miller, R. S. Assary, H. H. Wang, P. Redfern, H. Wu, J. B. Park, Y. K. Sun, S. Vajda, K. Amine and L. A. Curtiss, *Nat. Commun.*, 2014, **5**, 4895.
6 D. Oh, J. Qi, Y. C. Lu, Y. Zhang, Y. Shao-Horn and A. M. Belcher, *Nat. Commun.*, 2013, **4**, 2756.
7 S. H. Oh, R. Black, E. Pomerantseva, J. H. Lee and L. F. Nazar, *Nat. Chem.*, 2012, **4**, 1004–1010.
8 W. Zhang, J. Zhang, N. Wang, K. Zhu, C. Yang, Y. Ai, F. Wang, Y. Tian, Y. Ma, Y. Ma, X. Zhang, L. Duan, D. Chao, F. Wang, D. Zhao and W. Li, *Nat. Sustainability*, 2024, **7**, 463–473.
9 C. L. Yang, L. N. Wang, P. Yin, J. Liu, M. X. Chen, Q. Q. Yan, Z. S. Wang, S. L. Xu, S. Q. Chu, C. Cui, H. Ju, J. Zhu, Y. Lin, J. Shui and H. W. Liang, *Science*, 2021, **374**, 459–464.
10 W. Zhao, F. Xu, L. Liu, M. Liu and B. Weng, *Adv. Mater.*, 2023, **35**, e2308060.
11 Y. Zhu, Z. Wang, J. Gao, R. Sun, L. Yin, C. Wang and Z. Zhang, *Inorg. Chem. Front.*, 2023, **10**, 4252–4265.
12 X. Yi, X. Liu, W. Pan, B. Qin, J. Fang, K. Jiang, S. Deng, Y. Meng, D. Y. C. Leung and Z. Wen, *ACS Catal.*, 2022, **12**, 5048–5059.
13 Y. Li, Y. Li, Y. Ding, J. Ma, P. Das, B. Zhang, Z.-S. Wu and X. Bao, *Chem. Catal.*, 2023, **3**, 100658.
14 D. Cao, L. Zheng, Y. Wang, Y. Dong, Q. Li, Y. Li, X. Wang, Y. Bai, G. Tan and C. Wu, *Energy Storage Mater.*, 2022, **51**, 806–814.
15 S. Qiao, H. Shou, W. Xu, Y. Cao, Y. Zhou, Z. Wang, X. Wu, Q. He and L. Song, *Energy Environ. Sci.*, 2023, **16**, 5842–5851.
16 R. Mukherjee, A. V. Thomas, D. Datta, E. Singh, J. Li, O. Eksik, V. B. Shenoy and N. Koratkar, *Nat. Commun.*, 2014, **5**, 3710.
17 J. Liang, J. Liu, L. Guo, W. Wang, C. Wang, W. Gao, X. Guo, Y. He, G. Yang, S. Yasuda, B. Liang and N. Tsubaki, *Nat. Commun.*, 2024, **15**, 512.
18 Z. Tong, C. Lv, Y. Zhou, Z.-W. Yin, Z.-P. Wu and J.-T. Li, *Energy Storage Mater.*, 2024, **67**, 103301.
19 Z. Jiang, Y. Huang, Z. Zhu, S. Gao, Q. Lv and F. Li, *Proc. Natl. Acad. Sci. U. S. A.*, 2022, **119**, e2202835119.
20 S. Dong, S. Yang, Y. Chen, C. Kuss, G. Cui, L. R. Johnson, X. Gao and P. G. Bruce, *Joule*, 2022, **6**, 185–192.
21 Z. Li, X. Wu, J. Wang, H. Zhang, Y. Qin, Y. Qiao and S.-G. Sun, *J. Mater. Chem. A*, 2024, **12**, 15558–15579.

22 Y. Huang, H. Fang, J. Geng, T. Zhang, W. Hu and F. Li, *J. Am. Chem. Soc.*, 2024, **146**, 26516–26524.
23 J. Guo, X. Meng, Q. Wang, Y. Zhang, S. Yan and S. Luo, *Batteries*, 2024, **10**, 260.
24 E. L. Littauer and K. C. Tsai, *J. Am. Chem. Soc.*, 1976, **123**, 771–776.
25 T. Ogasawara, A. Débart, M. Holzapfel, P. Novák and P. G. Bruce, *J. Am. Chem. Soc.*, 2006, **126**, 1390–1393.
26 J. Xiao, D. Mei, X. Li, W. Xu, D. Wang, G. L. Graff, W. D. Bennett, Z. Nie, L. V. Saraf, I. A. Aksay, J. Liu and J. G. Zhang, *Nano Lett.*, 2011, **11**, 5071–5078.
27 J. L. Shui, N. K. Karan, M. Balasubramanian, S. Y. Li and D. J. Liu, *J. Am. Chem. Soc.*, 2012, **134**, 16654–16661.
28 Z. Peng, S. A. Freunberger, Y. Chen and P. G. Bruce, *Science*, 2012, **337**, 563–566.
29 Z. Jian, P. Liu, F. Li, P. He, X. Guo, M. Chen and H. Zhou, *Angew. Chem., Int. Ed.*, 2014, **53**, 442–446.
30 Q. Li, R. Cao, J. Cho and G. Wu, *Phys. Chem. Chem. Phys.*, 2014, **16**, 13568–13582.
31 Q. Li, P. Xu, W. Gao, S. Ma, G. Zhang, R. Cao, J. Cho, H. L. Wang and G. Wu, *Adv. Mater.*, 2014, **26**, 1378–1386.
32 D. Wu, Z. Guo, X. Yin, Q. Pang, B. Tu, L. Zhang, Y. G. Wang and Q. Li, *Adv. Mater.*, 2014, **26**, 3258–3262.
33 T. Liu, M. Leskes, W. Yu, A. J. Moore, L. Zhou, P. M. Bayley, G. Kim and C. P. Grey, *Science*, 2015, **350**, 530–533.
34 J. Lu, Y. J. Lee, X. Luo, K. C. Lau, M. Asadi, H. H. Wang, S. Brombosz, J. Wen, D. Zhai, Z. Chen, D. J. Miller, Y. S. Jeong, J. B. Park, Z. Z. Fang, B. Kumar, A. Salehi-Khojin, Y. K. Sun, L. A. Curtiss and K. Amine, *Nature*, 2016, **529**, 377–382.
35 C. Y. K. C. Xia and L. F. Nazar, *Science*, 2018, **361**, 777–781.
36 X. Hu, G. Luo, Q. Zhao, D. Wu, T. Yang, J. Wen, R. Wang, C. Xu and N. Hu, *J. Am. Chem. Soc.*, 2020, **142**, 16776–16786.
37 P. Wang, Y. Ren, R. Wang, P. Zhang, M. Ding, C. Li, D. Zhao, Z. Qian, Z. Zhang, L. Zhang and L. Yin, *Nat. Commun.*, 2020, **11**, 1576.
38 Y. Li, J. Cai, J. Zhang, Z. Chen, G. Wang, Q. Chen and M. Chen, *Adv. Energy Mater.*, 2023, **13**, 2204114.
39 Z. Sun, X. Lin, C. Wang, Y. Tan, W. Dou, A. Hu, J. Cui, J. Fan, R. Yuan, M. Zheng and Q. Dong, *Adv. Mater.*, 2024, **36**, e2404319.
40 E. Zhang, A. Dong, K. Yin, C. Ye, Y. Zhou, C. Tan, M. Li, X. Zheng, Y. Wang, X. Gao, H. Li, D. Wang and S. Guo, *J. Am. Chem. Soc.*, 2024, **146**, 2339–2344.
41 X. Y. Yuan, D. H. Guan, X. X. Wang, J. Y. Li, C. L. Miao and J. J. Xu, *Angew. Chem., Int. Ed.*, 2025, e202421361, DOI: **10.1002/anie.202421361**.
42 A. Mao, J. Li, J. H. Li, H. Liu and C. Lian, *J. Phys. Chem. Lett.*, 2024, **15**, 5501–5509.
43 Q. Xiong, G. Huang and X. B. Zhang, *Angew. Chem., Int. Ed.*, 2020, **59**, 19311–19319.
44 M. Huang, N. Wang, M. Xie, Y. Fu, Z. Li, Y. Lu and Q. Liu, *Adv. Funct. Mater.*, 2025, 2420678, DOI: **10.1002/adfm.202420678**.
45 Y. Qiu, G. Li, H. Zhou, G. Zhang, L. Guo, Z. Guo, R. Yang, Y. Fan, W. Wang, Y. Du and F. Dang, *Adv. Sci.*, 2023, **10**, 2300482.
46 C. Tan, D. Cao, L. Zheng, Y. Shen, L. Chen and Y. Chen, *J. Am. Chem. Soc.*, 2022, **144**, 807–815.
47 Q. Han, W. Guo, X. He, T. Liu, X. Liu, X. Zhu, T. Bian, L. Jiang, J. Lu and Y. Zhao, *Joule*, 2022, **6**, 381–398.
48 Y. Wang and Y. C. Lu, *Angew. Chem., Int. Ed.*, 2019, **58**, 6962–6966.
49 Y. Wang and Y.-C. Lu, *Energy Storage Mater.*, 2020, **28**, 235–246.
50 Y. Hase, T. Uyama, K. Nishioka, J. Seki, K. Morimoto, N. Ogihara, Y. Mukouyama and S. Nakanishi, *J. Am. Chem. Soc.*, 2022, **144**, 1296–1305.
51 Z. Jiang and A. M. Rappe, *J. Am. Chem. Soc.*, 2022, **144**, 22150–22158.
52 S. J. Kang, M. Hong, J. H. Won, B. Han, J. K. Kang and H. M. Jeong, *Adv. Energy Mater.*, 2024, **15**, 2402651.
53 H. Wong, T. Liu, M. Tamtaji, X. Huang, T. W. Tang, M. D. Hossain, J. Wang, Y. Cai, Z. Liu, H. Liu, K. Amine, W. A. Goddard and Z. Luo, *Nano Energy*, 2024, **121**, 109279.
54 F. Cheng and J. Chen, *Nat. Chem.*, 2012, **4**, 962–963.
55 S. J. Kang, T. Mori, S. Narizuka, W. Wilcke and H. C. Kim, *Nat. Commun.*, 2014, **5**, 3937.
56 J. J. Xu, Z. L. Wang, D. Xu, L. L. Zhang and X. B. Zhang, *Nat. Commun.*, 2013, **4**, 2438.
57 L. Johnson, C. Li, Z. Liu, Y. Chen, S. A. Freunberger, P. C. Ashok, B. B. Praveen, K. Dholakia, J. M. Tarascon and P. G. Bruce, *Nat. Chem.*, 2014, **6**, 1091–1099.
58 J. Wang, L. Ma, J. Xu, Y. Xu, K. Sun and Z. Peng, *SusMat*, 2021, **1**, 345–358.
59 Y. Wang, L. Hao and M. Bai, *Appl. Energy*, 2022, **317**, 119189.
60 Z. Peng, S. A. Freunberger, L. J. Hardwick, Y. Chen, V. Giordani, F. Barde, P. Novak, D. Graham, J. M. Tarascon and P. G. Bruce, *Angew. Chem., Int. Ed.*, 2011, **50**, 6351–6355.
61 P. Zhang, B. Han, X. Yang, Y. Zou, X. Lu, X. Liu, Y. Zhu, D. Wu, S. Shen, L. Li, Y. Zhao, J. S. Francisco and M. Gu, *J. Am. Chem. Soc.*, 2022, **144**, 2129–2136.
62 X. Cao, C. Wei, X. Zheng, K. Zeng, X. Chen, M. H. Rummeli, P. Strasser and R. Yang, *Energy Storage Mater.*, 2022, **50**, 355–364.
63 D. Zhai, H. H. Wang, J. Yang, K. C. Lau, K. Li, K. Amine and L. A. Curtiss, *J. Am. Chem. Soc.*, 2013, **135**, 15364–15372.
64 H. Zheng, D. Xiao, X. Li, Y. Liu, Y. Wu, J. Wang, K. Jiang, C. Chen, L. Gu, X. Wei, Y. S. Hu, Q. Chen and H. Li, *Nano Lett.*, 2014, **14**, 4245–4249.
65 J. Wang, Y. Zhang, L. Guo, E. Wang and Z. Peng, *Angew. Chem., Int. Ed.*, 2016, **55**, 5201–5205.
66 Y. Liu, J. Cai, J. Zhou, Y. Zang, X. Zheng, Z. Zhu, B. Liu, G. Wang and Y. Qian, *eScience*, 2022, **2**, 389–398.
67 O. Gerbig, R. Merkle and J. Maier, *Adv. Mater.*, 2013, **25**, 3129–3133.

68 T. Liu, J. P. Vivek, E. W. Zhao, J. Lei, N. Garcia-Araez and C. P. Grey, *Chem. Rev.*, 2020, **120**, 6558–6625.
69 F. Tian, M. D. Radin and D. J. Siegel, *Chem. Mater.*, 2014, **26**, 2952–2959.
70 M. D. Radin and D. J. Siegel, *Energy Environ. Sci.*, 2013, **6**, 2370.
71 B. D. McCloskey, R. Scheffler, A. Speidel, G. Girishkumar and A. C. Luntz, *J. Phys. Chem. C*, 2012, **116**, 23897–23905.
72 S. P. Ong, Y. Mo and G. Ceder, *Phys. Rev. B: Condens. Matter Mater. Phys.*, 2012, **85**, 081105.
73 A. Dunst, V. Epp, I. Hanzu, S. A. Freunberger and M. Wilkening, *Energy Environ. Sci.*, 2014, **7**, 2739–2752.
74 K. P. C. Yao, M. Risch, S. Y. Sayed, Y.-L. Lee, J. R. Harding, A. Grimaud, N. Pour, Z. Xu, J. Zhou, A. Mansour, F. Bardé and Y. Shao-Horn, *Energy Environ. Sci.*, 2015, **8**, 2417–2426.
75 M.-C. Sung, G.-H. Lee and D.-W. Kim, *Energy Storage Mater.*, 2023, **60**, 102829.
76 J. Chen, E. Quattrocchi, F. Ciucci and Y. Chen, *Chem*, 2023, **9**, 2267–2281.
77 C. Xu, A. Ge, K. Kannari, B. Peng, M. Xue, B. Ding, K.-i. Inoue, X. Zhang and S. Ye, *ACS Energy Lett.*, 2023, **8**, 1289–1299.
78 A. Kushima, T. Koido, Y. Fujiwara, N. Kuriyama, N. Kusumi and J. Li, *Nano Lett.*, 2015, **15**, 8260–8265.
79 Y. Wang, Z. Liang, Q. Zou, G. Cong and Y.-C. Lu, *J. Phys. Chem. C*, 2016, **120**, 6459–6466.
80 H. Zhou, L. Guo, R. Zhang, L. Xie, Y. Qiu, G. Zhang, Z. Guo, B. Kong and F. Dang, *Adv. Funct. Mater.*, 2023, **33**, 2304154.
81 H. Xu, X. Wang, G. Tian, F. Fan, X. Wen, P. Liu and C. Shu, *ACS Nano*, 2024, **18**, 27804–27816.
82 Y. Zhang, S. Zhang, H. Li, Y. Lin, M. Yuan, C. Nan and C. Chen, *Nano Lett.*, 2023, **23**, 9119–9125.
83 D. Zhang, G. Zhang, R. Liu, R. Yang, X. Li, X. Zhang, H. Yu, P. Zhang, B. W. Li, H. Hou, Z. Guo and F. Dang, *Adv. Funct. Mater.*, 2024, **35**, 2414679.
84 Y. Zhang, S. Zhang, J. Ma, X. Chen, C. Nan and C. Chen, *Angew. Chem., Int. Ed.*, 2023, **62**, e202218926.
85 S. Cho, H. Jung, M. Park, L. Lyu and Y.-M. Kang, *ACS Energy Lett.*, 2024, **9**, 2848–2857.
86 K. Teng, W. Tang, R. Qi, B. Li, Y. Deng, M. Zhou, M. Wu, J. Zhang, R. Liu and L. Zhang, *Catal. Today*, 2023, **409**, 23–30.
87 Z. Su, I. Temprano, N. Folastre, V. Vanpeene, J. Villanova, G. Gachot, E. V. Shevchenko, C. P. Grey, A. A. Franco and A. Demortiere, *Small Methods*, 2024, **8**, e2300452.
88 F. Xiao, Y. Meng, Z. Lin, Y. Lei, X. Chen, J. Zhang, H. Lu, Y. Tong, G. Liu and J. Xu, *Carbon*, 2022, **189**, 404–412.
89 X. Zheng, M. Yuan, J. Xu, Z. Li, C. Nan and G. Sun, *Nano Res.*, 2023, **17**, 4100–4107.
90 R. Zheng, D. Du, Y. Yan, S. Liu, X. Wang and C. Shu, *Adv. Funct. Mater.*, 2024, **34**, 2316440.
91 R. Huang, J. Chen, X. Chen, T. Yu, H. Yu, K. Li, B. Li and S. Yin, *Chin. J. Struct. Chem.*, 2023, **42**, 100171.
92 F. Yang, Y. Yao, Y. Xu, C. Wang, M. Wang, J. Ren, C. Zhang, F. Wu and J. Lu, *Carbon Energy*, 2023, **6**, e372.
93 S. Wen, B. Liu, W. Li, T. Liang, X. Li, D. Yi, B. Luo, L. Zhi, D. Liu and B. Wang, *Adv. Funct. Mater.*, 2022, **32**, 2203960.
94 Z. Lian, Y. Lu, S. Ma, Z. Li and Q. Liu, *Chem. Eng. J.*, 2022, **445**, 136852.
95 B. Wang, C. Liu, L. Yang, Q. Wu, X. Wang and Z. Hu, *Nano Res.*, 2022, **15**, 4132–4136.
96 Y. Pan, A. Hu, R. Xu, J. Chen, B. Yang, T. Li, K. Li, Y. Li, Z. W. Seh and J. Long, *ACS Sustainable Chem. Eng.*, 2024, **12**, 17177–17189.
97 X. Cao, M. Tian, Z. Sun, X. Zheng, K. Zeng, P. Strasser and R. Yang, *ACS Sustainable Chem. Eng.*, 2023, **11**, 10640–10648.
98 T. Yang, Y. Xia, T. Mao, Q. Ding, Z. Wang, Z. Hong, J. Han, D. L. Peng and G. Yue, *Adv. Funct. Mater.*, 2022, **32**, 2209876.
99 Z. Mohamed, Q. Zhou, K. Zhu, G. Zhang, W. Xu, P. J. Chimtali, Y. Cao, H. Xu, Z. Yan, Y. Wang, H. Akhtar, A. Al-Mahgari, X. Wu, C. Wang and L. Song, *Adv. Funct. Mater.*, 2024, **35**, 2410091.
100 H. Huang, C. Cheng, G. Zhang, L. Guo, G. Li, M. Pan, F. Dang and X. Mai, *Adv. Funct. Mater.*, 2022, **32**, 2111546.
101 Z. Sun, X. Zhao, W. Qiu, B. Sun, F. Bai, J. Liu and T. Zhang, *Adv. Mater.*, 2023, **35**, e2210867.
102 W. Yu, Z. Shen, T. Yoshii, S. Iwamura, M. Ono, S. Matsuda, M. Aoki, T. Kondo, S. R. Mukai, S. Nakanishi and H. Nishihara, *Adv. Energy Mater.*, 2023, **14**, 2303055.
103 Y. Wu, H. Ding, T. Yang, Y. Xia, H. Zheng, Q. Wei, J. Han, D. L. Peng and G. Yue, *Adv. Sci.*, 2022, **9**, e2200523.
104 W. Yu, T. Yoshii, A. Aziz, R. Tang, Z. Z. Pan, K. Inoue, M. Kotani, H. Tanaka, E. Scholtzova, D. Tunega, Y. Nishina, K. Nishioka, S. Nakanishi, Y. Zhou, O. Terasaki and H. Nishihara, *Adv. Sci.*, 2023, **10**, e2300268.
105 C. Zhao, Z. Yan, B. Zhou, Y. Pan, A. Hu, M. He, J. Liu and J. Long, *Angew. Chem., Int. Ed.*, 2023, **62**, e202302746.
106 Q. Lv, Z. Zhu, Y. Ni, J. Geng and F. Li, *Angew. Chem., Int. Ed.*, 2022, **61**, e202114293.
107 Y. Zhou, Q. Gu, K. Yin, Y. Li, L. Tao, H. Tan, Y. Yang and S. Guo, *Angew. Chem., Int. Ed.*, 2022, **61**, e202201416.
108 M. Huang, L. Song, N. Wang, Y. Fu, R. Ren, Z. Li, Y. Lu, J. Xu and Q. Liu, *Angew. Chem., Int. Ed.*, 2025, **64**, e202414893.
109 M. Zhao, J. Sun, T. Luo, Y. Yan, W. Huang and J. M. Lee, *Small*, 2024, **20**, e2309351.
110 L. Huang, L. Zhang, M. Liu, Q. Zhang, Z. Chen, L. Zheng, Z. Cui, Z. Zhang and S. Liao, *Energy Storage Mater.*, 2023, **61**, 102874.
111 Q. Lv, Z. Zhu, Y. Ni, B. Wen, Z. Jiang, H. Fang and F. Li, *J. Am. Chem. Soc.*, 2022, **144**, 23239–23246.
112 Y. Zhou, Q. Gu, Y. Xin, X. Tang, H. Wu and S. Guo, *Nano Lett.*, 2023, **23**, 10600–10607.
113 J. Qiu, Y. Lin, S. Zhang, J. Ma, Y. Zhang, M. Yuan, G. Sun and C. Nan, *Nano Res.*, 2023, **16**, 6798–6804.
114 Y. Xia, L. Wang, G. Gao, T. Mao, Z. Wang, X. Jin, Z. Hong, J. Han, D. L. Peng and G. Yue, *Nano-Micro Lett.*, 2024, **16**, 258.

115 Y. Zhou, Q. Gu, K. Yin, L. Tao, Y. Li, H. Tan, Y. Yang and S. Guo, *Proc. Natl. Acad. Sci. U. S. A.*, 2023, **120**, e2301439120.
116 J. Tian, Y. Rao, W. Shi, J. Yang, W. Ning, H. Li, Y. Yao, H. Zhou and S. Guo, *Angew. Chem., Int. Ed.*, 2023, **62**, e202310894.
117 B. Sun, W. Zheng, C. Kang, B. Xie, Z. Qian, Y. Wang, S. Ye, S. Lou, F. Kong, B. Mei, C. Du, P. Zuo, J. Xie and G. Yin, *Small*, 2023, **19**, e2207461.
118 X. Wang, D. Du, Y. Yan, L. Ren, H. Xu, X. Wen, T. Zeng, G. Tian, S. Liu, F. Fan and C. Shu, *Energy Storage Mater.*, 2023, **63**, 103033.
119 Y. Li, J. Qin, Y. Ding, J. Ma, P. Das, H. Liu, Z.-S. Wu and X. Bao, *ACS Catal.*, 2022, **12**, 12765–12773.
120 X. X. Wang, D. H. Guan, F. Li, M. L. Li, L. J. Zheng and J. J. Xu, *Adv. Mater.*, 2022, **34**, e2104792.
121 H. Xu, R. Zheng, D. Du, L. Ren, X. Wen, X. Wang, G. Tian and C. Shu, *Small*, 2023, **19**, e2206611.
122 S. Ding, L. Wu and X. Yuan, *Chem. Eng. J.*, 2023, **478**, 147473.
123 F. Xiao, Q. Bao, C. Sun, Y. Li, D. Cui, Q. Wang, F. Dang, H. Yu and G. Lian, *Adv. Energy Mater.*, 2024, **14**, 2303766.
124 H. Yu, G. Zhang, D. Zhang, R. Yang, X. Li, X. Zhang, G. Lian, H. Hou, Z. Guo, C. Hou, X. Yang and F. Dang, *Adv. Energy Mater.*, 2024, **14**, 2401509.
125 X. Li, G. Zhang, D. Zhang, R. Yang, H. Yu, X. Zhang, G. Lian, H. Hou, Z. Guo, C. Hou, X. Yang and F. Dang, *Energy Environ. Sci.*, 2024, **17**, 8198–8208.
126 C. Sun, X. Cui, F. Xiao, D. Cui, Q. Wang, F. Dang, H. Yu and G. Lian, *Small*, 2024, **20**, e2400010.
127 X. Han, L. Zhao, J. Wang, Y. Liang and J. Zhang, *Adv. Mater.*, 2023, **35**, e2301897.
128 G. Tian, H. Xu, X. Wang, X. Wen, T. Zeng, S. Liu, F. Fan, W. Xiang and C. Shu, *Nano Energy*, 2023, **117**, 108863.
129 X. Wen, D. Du, L. Ren, H. Xu, R. Li, C. Zhao and C. Shu, *Chem. Eng. J.*, 2022, **442**, 136311.
130 Y. Zhao, W. Tang, W. Liu, X. Kong, D. Zhang, H. Luo, K. Teng and R. Liu, *Small*, 2023, **19**, e2205532.
131 P. Zhang, X. Hui, Y. Nie, R. Wang, C. Wang, Z. Zhang and L. Yin, *Small*, 2023, **19**, e2206742.
132 J. Zheng, W. Zhang, R. Wang, J. Wang, Y. Zhai and X. Liu, *Small*, 2023, **19**, e2204559.
133 Y. Zhao, Z. Wang, S. Guan, Y. Gao, S. Gong, G. Han, P. Gao, S. Lou, Y. Zhu and X. Li, *Chem. Eng. J.*, 2024, **500**, 156972.
134 G. Tian, H. Xu, X. Wang, X. Wen, P. Liu, S. Liu, T. Zeng, F. Fan, S. Wang, C. Wang, C. Zeng and C. Shu, *ACS Nano*, 2024, **18**, 11849–11862.
135 P. Liu, H. Xu, X. Wang, G. Tian, X. Yu, C. Wang, C. Zeng, S. Wang, F. Fan, S. Liu and C. Shu, *Small*, 2024, **20**, e2404483.
136 Z. Sun, Y. Hu, J. Zhang, N. Zhou, M. Li, H. Liu, B. Huo, M. Chao and K. Zeng, *Appl. Catal., B*, 2024, **351**, 123984.
137 H. Liang, L. Jia, F. Chen, S. Jing and P. Tsiakaras, *Appl. Catal., B*, 2022, **317**, 121698.
138 H. Liang, Z. Gai, F. Chen, S. Jing, W. Kan, B. Zhao, S. Yin and P. Tsiakaras, *Appl. Catal., B*, 2023, **324**, 122203.
139 D. Wu, S. Wu, G. Zhang, C. Hui, D. Cao, S. Guo, H. Feng, Q. Wang, S. Cheng, P. Cui and Z. Yang, *Small*, 2023, **19**, e2206455.
140 Z. Liu, H. Xu, X. Wang, G. Tian, D. Du and C. Shu, *Battery Energy*, 2024, **3**, 20230053.
141 J. Feng, A. Abbas, L. Zhao, H. Sun, Z. Li, C. Wang and H. Wang, *Small*, 2024, **20**, e2406081.
142 M. C. Sung, C. H. Kim, B. Hwang and D. W. Kim, *Carbon Energy*, 2024, **6**, e550.
143 L. Zhao, J. Feng, A. Abbas, C. Wang and H. Wang, *Small*, 2023, **19**, e2302953.
144 L. Ren, X. Wen, D. Du, Y. Yan, H. Xu, T. Zeng and C. Shu, *Chem. Eng. J.*, 2023, **462**, 142288.
145 X. Wang, D. Du, H. Xu, Y. Yan, X. Wen, L. Ren and C. Shu, *Chem. Eng. J.*, 2023, **452**, 139524.
146 Z. Zhou, L. Zhao, J. Wang, Y. Zhang, Y. Li, S. Shoukat, X. Han, Y. Long and Y. Liu, *Small*, 2023, **19**, e2302598.
147 Y. Pan, R. Xu, A. Hu, C. Zhao, R. Li, B. Zhou, J. Liu and J. Long, *Batteries Supercaps*, 2024, **7**, e202300609.
148 S. Wang, S. Yao, F. Zhang, K. Ji, Y. Ji, J. Li, W. Fu, Y. Liu, J. Yang, R. Liu, J. Xie, Z. Yang and Y. M. Yan, *Angew. Chem., Int. Ed.*, 2025, **64**, e202415997.
149 Z. Zhang, P. Ma, L. Luo, X. Ding, S. Zhou and J. Zeng, *Angew. Chem., Int. Ed.*, 2023, **62**, e202216837.
150 S. Ding, L. Wu, F. Zhang and X. Yuan, *Small*, 2023, **19**, e2300602.
151 Z. Lian, Y. Lu, S. Zhao, Z. Li and Q. Liu, *Adv. Sci.*, 2023, **10**, e2205975.
152 L.-J. Zheng, Y. Yan, X.-X. Wang, L.-N. Song, H.-F. Wang and J.-J. Xu, *Energy Storage Mater.*, 2023, **56**, 331–341.
153 M. Li, X. Wang, K. Liu, H. Sun, D. Sun, K. Huang, Y. Tang, W. Xing, H. Li and G. Fu, *Adv. Mater.*, 2023, **35**, e2302462.
154 X. Wang, M. Li, P. Wang, D. Sun, L. Ding, H. Li, Y. Tang and G. Fu, *Small Methods*, 2023, **7**, e2300100.
155 R. T. Hannagan, G. Giannakakis, M. Flytzani-Stephanopoulos and E. C. H. Sykes, *Chem. Rev.*, 2020, **120**, 12044–12088.
156 X. Wu, W. Yu, W. Xu, Y. Zhang, S. Guan, Z. Zhang, S. Li, H. Wang, X. Wang, L. Zhang, C.-W. Nan and L. Li, *Composites, Part B*, 2022, **234**, 109727.
157 R. Li, A. Hu, C. Zhao, B. Zhou, M. He, Y. Fan, J. Chen, Z. Yan, Y. Pan and J. Long, *Chem. Eng. J.*, 2023, **452**, 139162.
158 Y. Long, Q. Li, Z. Zhang, Q. Zeng, D. Liu, L. Zhao, Y. Liu, Y. Li, Y. Zhang, K. Ji, Z. Zhou, X. Han and J. Wang, *Small*, 2024, **20**, e2304882.
159 S. Zhang, J. Qiu, Y. Zhang, Y. Lin, R. Liu, M. Yuan, G. Sun and C. Nan, *Small*, 2022, **18**, e2201150.
160 S.-S. Li, X.-L. Zhao, Y.-S. Liu, J.-J. Liu, K.-X. Wang and J.-S. Chen, *Energy Storage Mater.*, 2023, **56**, 506–514.
161 L. Guo, L. Tan, A. Xu, G. Li, G. Zhang, R. Liu, J. Wang, Y. Du and F. Dang, *Energy Storage Mater.*, 2022, **50**, 96–104.
162 G. Zhang, G. Li, J. Wang, H. Tong, J. Wang, Y. Du, S. Sun and F. Dang, *Adv. Energy Mater.*, 2022, **12**, 2103910.

163 G. Zhang, C. Liu, L. Guo, R. Liu, L. Miao and F. Dang, *Adv. Energy Mater.*, 2022, **12**, 2200791.
164 X. Zhang, G. Zhang, R. Yang, D. Zhang, G. Lian, C. Hou, J. Ren, H. Hou, Z. Guo and F. Dang, *Energy Storage Mater.*, 2024, **69**, 103392.
165 R. Yang, J. Li, D. Zhang, X. Zhang, X. Li, H. Yu, Z. Guo, C. Hou, G. Lian and F. Dang, *Chin. Chem. Lett.*, 2024, **35**, 109595.
166 L. Li, F. Ma, C. Jia, Q. Li, X. He, J. Sun, R. Jiang, Z. Lei and Z. H. Liu, *Adv. Sci.*, 2023, **10**, e2301682.
167 C. Jia, F. Zhang, N. Zhang, Q. Li, X. He, J. Sun, R. Jiang, Z. Lei and Z. H. Liu, *ACS Nano*, 2023, **17**, 1713–1722.
168 S. Xia, Y. Yang, Q. Jia, M. Shang, L. Li, S. Chen and W. Zhang, *Inorg. Chem. Front.*, 2024, **11**, 3538–3547.
169 L. J. Zheng, L. N. Song, X. X. Wang, S. Liang, H. F. Wang, X. Y. Du and J. J. Xu, *Angew. Chem., Int. Ed.*, 2023, **62**, e202311739.
170 Y. Wang, L. N. Song, Y. F. Wang, X. X. Wang, J. Y. Wu, Y. Sun and J. J. Xu, *Adv. Funct. Mater.*, 2024, **34**, 2405222.
171 X. Li, Y. Su, Y. Ma, L. Wei, Y. He, Y. Gu, S. Mei, Q. Mu, C. Peng, Y. Peng and Z. Deng, *Appl. Catal., B*, 2023, **337**, 122964.
172 Y. Tao, T. Wang, X. Yu, K. Gong, H. Gong, H. Chen, X. Fan, A. Zhang, X. Huang, K. Chang and J. He, *Chem. Sci.*, 2024, **15**, 17073–17083.
173 X. Yu, H. Gong, B. Gao, X. Fan, P. Li, X. Huang, K. Chang, T. Wang and J. He, *Chem. Eng. J.*, 2022, **449**, 137774.
174 R. Cao, Y. Cui, G. Huang, W. Liu, J. Liu and X. Zhang, *Nano Res.*, 2022, **16**, 8405–8410.
175 M. Wang, J. Chen, Z. Tian, W. Dai, B. Cui, X. Cui, D. Wang, Y. Xiao, X. Lian, C. Jiang, H. Yang, Y. Wang, Z. Sun, Y. Ding, Y.-Y. Sun, J. Zhang and W. Chen, *Energy Environ. Sci.*, 2023, **16**, 523–534.
176 F. Li, M. L. Li, H. F. Wang, X. X. Wang, L. J. Zheng, D. H. Guan, L. M. Chang, J. J. Xu and Y. Wang, *Adv. Mater.*, 2022, **34**, e2107826.
177 Z. Zhu, Q. Lv, Y. Ni, S. Gao, J. Geng, J. Liang and F. Li, *Angew. Chem., Int. Ed.*, 2022, **61**, e202116699.
178 H. Yu, D. Liu, Z. Fu, S. Wang, X. Zuo, X. Feng and Y. Zhang, *Angew. Chem., Int. Ed.*, 2024, **63**, e202401272.
179 B. Wen, Y. Huang, Z. Jiang, Y. Wang, W. Hua, S. Indris and F. Li, *Adv. Mater.*, 2024, **36**, e2405440.
180 J. Zhang, Z. Zhou, Y. Wang, Q. Chen, G. Hou and Y. Tang, *Nano Energy*, 2022, **102**, 107655.
181 H. Jiao, G. Sun, Y. Wang, Z. Zhang, Z. Wang, H. Wang, H. Li and M. Feng, *Chin. Chem. Lett.*, 2022, **33**, 4008–4012.
182 C. Dang, S. He, Y. Liu, L. Zhao, A. Shan, M. Li, L. Kong and L. Gao, *Chem. Eng. J.*, 2023, **476**, 146775.
183 G. Wang, Y. Yang, Q. Zhang, Z. Xie and Z. Zhou, *Coord. Chem. Rev.*, 2024, **511**, 215879.
184 W. Wang, T. Yu, Y. Cheng, X. Lei, B. Wang, R. Guo, X. Liu, J. You, X. Wang and H. Zhang, *Nano Energy*, 2024, **125**, 109550.
185 W. Wang and Y. C. Lu, *SusMat*, 2023, **3**, 146–159.
186 Z. Wang, Y. Li, C. Wu and S. C. E. Tsang, *Joule*, 2022, **6**, 1798–1825.
187 L. Jiang, L. Jiang, X. Luo, R. Li, Q. Zhou, W. Zeng, J. Yu, L. Chen and S. Mu, *eScience*, 2025, 100398.